Physics – Uspekhi **46** (1) 63 – 79 (2003)

REVIEWS OF TOPICAL PROBLEMS PACS numbers: 84.40.Ba, 92.10.Hm, **93.85.+q**

Physical mechanisms of aerospace radar imaging of the ocean

M G Bulatov, Yu A Kravtsov, O Yu Lavrova, K Ts Litovchenko, M I Mityagina, M D Raev, K D Sabinin, Yu G Trokhimovskiĭ, A N Churyumov, I V Shugan

DOI: 10.1070/PU2003v046n01ABEH001114

Contents

Abstract. Physical mechanisms of the radar imaging of the ocean surface are reviewed. The resonant and nonresonant mechanisms of microwave radiation scattering from the ocean surface are considered, analyzed, and compared based on 20 years of the authors' own theoretical and experimental work, and publications by other research teams. The experimental facts that cannot be explained by resonant scattering models are analyzed in detail, and in this connection the significant contribution of mesoscale breaking waves to scattering at grazing angles is justified. The characteristic features and most probable mechanisms of radar imaging of various mesoscale phenomena deep in the ocean and in the atmosphere are considered.

M G Bulatov, O Y Lavrova, K Ts Litovchenko, M I Mityagina, M D Raev, Yu G Trokhimovskiĭ, A N Churyumov
Space Research Institute, Russian Academy of Sciences,
ul. Profsoyuznaya 84/32, 117997 Moscow, Russian Federation
Tel. (7-095) 333 50 78. Fax (7-095) 333 10 56
E-mail: mityag@mx.iki.rssi.ru
Yu A Kravtsov Space Research Institute, Russian Academy of Sciences,
ul. Profsoyuznaya 84/32, 117997 Moscow, Russian Federation
Tel. (7-095) 333 52 79
Center of Space Research, Polish Academy of Sciences,
00716 Warsaw, Poland
E-mail: kravtsov@asp.iki.rssi.ru
K D Sabinin Space Research Institute, Russian Academy of Sciences,
ul. Profsoyuznaya 84/32, 117997 Moscow, Russian Federation
N N Andreev Acoustical Institute
ul. Shvernika 4, 117036 Moscow, Russian Federation
Tel. (7-095) 126 98 46
I V Shugan Institute of General Physics, Russian Academy of Sciences,
ul. Vavilova 38, 117942 Moscow, Russian Federation
Tel. (7-095) 135 82 34

Received 10 October 2001, revised 10 April 2002
Uspekhi Fizicheskikh Nauk **173** (1) 69 – 87 (2003)
Translated by Yu V Morozov; edited by A Radzig

1. Introduction

Radar images of the sea surface obtained from aircrafts and satellites carry information about various phenomena that occur both in the near-surface layer and in the depths of the ocean. It goes without saying that microwaves penetrate a water column by as much as a few millimetres at the most; therefore, processes taking place in the ocean deeper than that are possible to visualize solely from their surface manifestations.

Radar images reveal first of all traces of *currents* and *eddies* in the ocean as well as *hydrologic fronts* or interfaces between bodies of sea water with different properties (temperature, salinity, density, color, various water suspensions and organic impurities). Currents, in their turn, depend on bottom topography (especially in shallow areas) which allows radar images to be used as sources of indirect information about the *bottom* relief. High-resolution radars produce images of *surface waves* or, more precisely, their large-scale component with characteristic lengths in excess of 20 – 40 m. Of special interest are surface manifestations of *internal waves* in the ocean. Moreover, radars can distinguish smoothed areas of an ocean surface or slicks, including those due to *oil pollution* or *surface-active substances*.

The ocean surface is subject not only to intrinsic oceanic processes but also to some atmospheric ones. Specifically, radar images show manifestations of a *near-surface wind* that affects the centimeter portion of the sea wave spectrum

(gravity-capillary waves) and thereby contributes to microwave scattering. Ripples on the ocean surface excited by the wind enable visualization of a variety of other atmospheric motions, such as *atmospheric fronts, atmospheric internal waves*, and atmospheric *convective cells* that form over the ocean under unstable air stratification, i.e., when sea surface temperature is higher than the air temperature close to it.

Finally, radar imaging provide information about *atmospheric precipitation* that can either promote or impair radio scattering due to the 'surface-smoothing' effect.

Ripples caused by the near-surface wind reflect both atmospheric and bulk oceanic processes that in some way or other modulate short gravity-capillary waves at the ocean surface; this effect is in turn manifested as modulation of a radar signal. In such a manner radar images of the ocean surface visualize both oceanic and atmospheric motions. This is a kind of natural Wilson chamber making it possible to observe phenomena hidden from view. Microwaves have a great advantage over electromagnetic waves of other frequency ranges because they can penetrate through cloud cover and thus render round-the-clock observations of the ocean possible regardless of weather conditions. Another advantage of microwaves, important for remote sensing of the ocean, lies in the fact that they *resonantly* interact with surface perturbations and thereby visualize such motions in the ocean that are impossible to observe using electromagnetic waves of other frequency ranges.

The importance of developing adequate methods for interpreting satellite images is emphasized in Ref. [1] as one of the topical problems that needs to be resolved to ensure the progress of space oceanology in Russia in the near future.

The main objective of this review is to analyze fundamental mechanisms governing the formation of radar images of the ocean. Elementary information about radars designed for aerospace sensing of the ocean is presented in Section 2, and a brief review of the microwave scattering mechanisms proposed thus far in Section 3. Special attention is given to nonresonant scattering mechanisms, the role of which has been grossly underestimated in recent years. With this in mind, Sections 4 – 8 are devoted to a detailed consideration of various phenomena and objects distinguishable in radar images of the sea surface, such as surface waves, currents, eddies and hydrologic fronts, internal waves, atmospheric movements, surface-active substances, oil slicks, etc. Materials for the analysis of these phenomena are borrowed from monographs concerned with remote sensing techniques [2 – 5] and other published materials on radar sensing of the ocean; also, they include results of theoretical and experimental studies performed at the Space Research Institute (Moscow) of the Russian Academy of Sciences.

During the last 30 years, these research activities were directed by professor V S Étkin who obtained very important data on radar and radiometry of the ocean. The works of V S Étkin in many respects laid the foundation for the high level of ocean remote sensing research achieved in this country. Valentin Semenovich Étkin would have been 70 on 28 June 2001. We would like to commemorate this date by publishing the present review.

A number of questions pertinent to ocean radar but having no direct relation to the production and interpretation of radar images remain beyond the scope of this review. These are radio altimetry, Doppler shift measurements, panoramic interferometry, etc. Also, we do not consider problems concerning the analysis of the radar images of sea ice.

2. Information about radars for observation of the ocean

2.1 Side-looking radars

Radars operating at wavelengths from 3 mm (the frequency $f = 100$ GHz) to 30 cm ($f = 1$ GHz) are used in oceanographic research. Normally, such radars are operated in the pulse mode although continuous emission is acceptable for some applications.

Radars placed on board aircraft are usually the *side-looking airborne radars* (SLAR). This variety of radar stations employs a side-looking antenna, i.e., one extended along the fuselage and whose beam provides a side 'viewing'. Let the axis x be aligned with the flight path, and the axis y be normal to x. Radar azimuthal resolution (in slant range) depends on pulse duration τ: at a typical pulse length of $\tau = 0.1$ μs, the resolution is $\Delta y = c\tau/2 = 15$ m, where c is the velocity of light.

The along-track resolution (axis x), i.e., in the direction of flight, is determined by the angular (azimuthal) width $\Delta\varphi$ of the directional pattern, which can be expressed as the ratio of wavelength λ to antenna length l_a:

$$\Delta\varphi \sim \frac{\lambda}{l_a} . \qquad (1)$$

At a wavelength $\lambda = 2$ cm and an antenna length $l_a = 6$ m (a rather large length for the airborne radar antenna), $\Delta\varphi \approx 1/300$ rad, with the resolution element $\Delta x = y\Delta\varphi/2 = 15$ m at a distance $y = 10$ km from the flight axis. Therefore, in the above example, the resolution element ('pixel') in plane x, y is a square measuring 15 m × 15 m.

A dual-polarization SLAR designated Nit' (thread in English), with which TU-134 aircraft-mounted laboratories are equipped [5], possesses approximately this resolution. This radar station operates in the short centimeter range (Ku-band: $\lambda = 2.25$ cm, radiation frequency $f = 13.3$ GHz) and has a peak power of 60 kW, pulse-repetition frequency 2 kHz, and pulse duration 110 ns. Two antennas, 6000 mm × 440 mm each, are installed on either side of the fuselage and used alternately to send and receive vertically (VV) and horizontally (HH) polarized signals. The pulse-repetition frequency for either polarization is 1 kHz. Viewing angles reckoned from the nadir lie between 72° and 84°, the spatial resolution element is 25 m × 25 m in size, and the antenna beam width $B = 0.0035$ rad. The width of a surveillance strip (illuminated area or swath) on either side of the aircraft is about 12.5 km for the aircraft's rated flight altitude of 2 km. The two surveillance strips are spaced approximately 12.5 km apart (Fig. 1).

For a satellite-borne SLAR, the size of a resolution element in the along-track direction (axis x) is much greater because the slant range R increases to 400 – 1000 km depending on the orbit altitude. For example, SLAR carried by the 'Okean O' (Ocean O) satellite possesses a resolution element of 1300 m × 2000 m.

2.2 Synthetic-aperture radars

The along-track resolution Δx can be improved by utilizing the 'aperture synthesis' technique that provides a tool for the specialized, coherent (i.e., phase-conserving) processing of back scattered signals recorded during a certain time Δt for which an aircraft or satellite moving at a speed v covers a

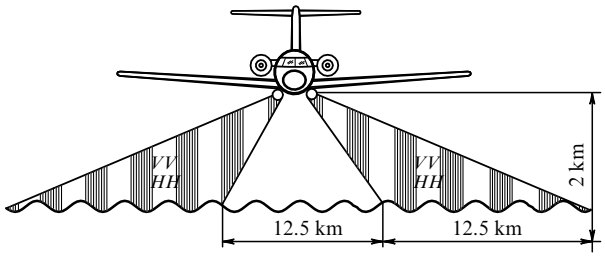

Figure 1. Geometry of radar sensing of underlying surface with a Nit' SLAR aboard the TU-134 aircraft-laboratory.

distance $v\Delta t$. Distance $\Delta l_{\text{synth}} = v\Delta t$ stands for the *synthesized* antenna length and may be hundreds and thousands of times greater than the physical l_a size of an airborne radar antenna.

At $\Delta l_{\text{synth}} = 5$ km, a wavelength of 5 cm, and slant range $R = 1000$ km, the resolution $\Delta x = R\Delta\varphi/2 = \lambda R/(2v\Delta t)$ derived from formula (1) is 5 m and compares favorably with that of satellite-borne optical devices. The very high resolution of synthetic-aperture radars (SAR) is coupled to their ability to operate through clouds and in the night-time. As mentioned above, it is their main advantage over optical and IR instruments.

Today, SARs are installed on European ERS-1 and ERS-2 satellites and the Canadian RADARSAT satellite. Some principal characteristics of these radars and those of SARs carried by Russian satellites 'Kosmos 1870' (Cosmos 1870) and 'Almaz' (Diamond), which were launched in 1987–1989 and 1992, respectively, are summarized in Table 1.

The synthetic-aperture radar SIR-C/X-SAR aboard the space shuttle 'Endeavour' provides an example of a highly informative tool for land and ocean surface surveillance with the aid of space-based imaging radars. The antenna of this radar station consists of three modules operating in the L-band (wavelength 23.5 cm), C-band (wavelength 5.8 cm), and X-band (wavelength 3 cm), respectively. L- and C-band images are obtained concurrently for vertical and horizontal polarizations of the sounding signal.

The principal parameters of the system are as follows: orbit altitude 225 km, ground resolution 30 m $\times$ 30 m, viewing angles (from the nadir) between 17° and 63°, swath width 15–90 km for L- and X-bands, and 15–40 km for the C-band.

Synthetic-aperture radars can be mounted not only on space vehicles but also on aircraft-laboratories. The most widely known instrument of this kind is SAR carried by a DC-8 aircraft owned by the Jet Propulsion Laboratory (Pasadena). Its principal characteristics are presented in Table 2. Readers interested in more complete information on satellite-borne radars are referred to handbooks [7, 8].

It is worth noting that SAR images are formed in a somewhat different way than images obtained by SLAR, radars on board ship and land-based radar systems. The fact is that, in the case of SAR, the usual modulation of Bragg scattering cross sections is supplemented by another mechanism, namely the Doppler shift frequency modulation. There is no detection of such a modulation in SLAR. In contrast, the orbital motion of an SAR unit enables it to 'view' surface waves even in the absence of scattering cross section fluctuations.

Space-based SARs operate at the angles of incidence from 20° to 60°. Due to this, nonresonant scattering effects are weak, and SAR images are formed largely through the Bragg scattering mechanism with the involvement of the Doppler effect. Doppler visualization of fluid motion undoubtedly facilitates observation. However, it is also associated with a negative manifestation of orbital motion. Specifically, SAR images exhibit 'beats' which are due to the interference between Doppler frequencies and perceived in a practical situation as a characteristic noise that makes it difficult to retrieve the spectra of surface waves. As a result, a spectrum

Table 1. Main characteristics of satellite-borne synthetic-aperture radars.

Characteristics	'Almaz'	ERS-1/2	RADARSAT
Orbit altitude, km	300–370 km	785 km	793–821 km
Inclination of orbit	73°	98.5°	98.6°
Sounding signal frequency	3.1 GHz	5.3 GHz	5.3 GHz
Sounding signal wavelength	9.6 cm	5.7 cm	5.7 cm
Polarization	*HH*	*VV*	*HH*
Pulse power of the transmitter	190 kW	4.8 kW	5 kW
Pulse duration	0.07–0.1 μs	37 μs	42 μs
Pulse repetition frequency	3000 Hz	1640–1720 Hz	1270–1390 Hz
Swath width	30–60 km	100 km	to 500 km
Signal/noise ratio	10 dB	8 dB	
Noncoherent accumulation	none	3-fold	1-, 2-, 4-, 8-fold
Spatial resolution			
— across track	22 m	25 m	to 9 m
— along track	25 m	25 m	to 9 m
Incidence angle in the middle of the surveillance strip	17°–62°	23°	10°–60°

Table 2. Principal characteristics of the SAR aboard the DC-8 aircraft-laboratory.

Band	P	L	C
Sounding signal frequency (for different ranges)	0.45 GHz	1.26 GHz	5.31 GHz
Sounding signal wavelength	67 cm	23 cm	5.7 cm
Polarization		Complete	
Spatial resolution along track	7.5 m	3.75 m	1.875 m
Spatial resolution across track		1 m	
Pulse duration		5 μs or 10 μs	
Pulse power of the transmitter	1 kW	6 kW	2 kW
Swath width		10 km (rated), 17 km (maximal)	
Angles of incidence		20°–60°	
Flight altitude		8 km	

of surface waves recorded by a coherent SAR that probes random surface motions is not identical with the initial one.

Formation of sea-surface SAR images has been considered in numerous publications both in this country and abroad (see, for instance, papers [9 – 13]).

2.3 Methods for processing radar images of the ocean

The standard procedure for the processing of radar images (RI) includes their interpretation, calibration, and normalization. In addition, spectral analysis of waves can be applied to study processes and phenomena that occur at the ocean surface.

Quality processing (interpretation) of RI is understood to be an explanation of the observable brightness contrasts, detection of signatures (i.e., structures of characteristic shape, size, and contrast), and correlation of signature shapes with certain typical forms created by known processes in the ocean and atmosphere. The interpretation is preceded by quantitative data processing that comprises determination of numerical parameters, such as contrast magnitudes, dimensions, and other geometric characteristics of the signatures.

The main calibration procedure is the conversion of image elements from arbitrary into absolute values of a microwave scattering cross section. The absolute values thus derived facilitate interpretation because the effects of different processes on a surface (hence, on radar backscatter) are as a rule modeled using values of microwave scattering cross sections.

The image brightnesses obtained by ERS spacecrafts are expressed in integers from 0 to 32768 for the two-byte representation, and from 0 to 255 for the one-byte format. As a rule, brightness is described by the square root of image intensity. For example, the following main rules of brightness conversion are worth mentioning for ERS.SAR.PRI products:

a pixel is directly proportional to the square root of image intensity;

intensity is proportional to the brightness β_0 of radar image;

brightness of radar image is directly proportional to the back reflection factor σ_0 divided by the sine of the angle of incidence.

Thus, one finds

$$[DN]^2 = K\beta_0 = K\,\frac{\sigma_0}{\sin\alpha} = K(\alpha)\,\sigma_0\,,$$

where DN is the initial image brightness, K is the gauge constant, α is the local viewing angle, and $K(\alpha)$ is the gauge constant depending on the local viewing angle:

$$K(\alpha) = K\,\frac{\sin\alpha_{\rm ref}}{\sin\alpha}\,,$$

where $\alpha_{\rm ref}$ is the reference local viewing angle (for ERS, $\alpha_{\rm ref} = 23^\circ$).

Gauge constants differ for various types of products; they are entered into the product heading together with other auxiliary information. Image brightnesses are converted into the scale of the normalized back scattering factor σ^0 using the formula

$$\sigma^0 = 20\,\log_{10}(DN) - K\,.$$

In certain cases, structures hardly discernible in an image because of poor contrast are possible to distinguish by making use of specialized radar-image-processing techniques, such as normalization. Of course, this method only permits the enhancement of contrast between visible anomalies of the image to better determine their shape, size, and position, but it is certainly unable to reveal what the radar image does not contain. The main operations of such processing are trend smoothing, filtration, and manipulation with histograms. This kind of data processing introduces, as a matter of necessity, a subjective element, the involvement of which depends on the visual quality of the image.

Normalization of radar images implies the following three operations:

azimuth-direction histogram adjusting or trend elimination (if appropriate);

contrast enhancement;

determination of geographic coordinates of the image and its transformation into the geographic projection.

By the *lateral trend* is meant the range dependence of the back scattering factor attributable to a change of σ^0 with varying viewing angle. The tilt of the lateral trend is wind-speed dependent. The trend can be eliminated in two ways, based on a theoretical dependence of σ^0 on the viewing angle and using actual sensing data. In the former case, only a more or less precise wind speed and direction need to be known to derive the theoretical dependence and use it to introduce necessary corrections. In the latter case, the lateral trend is eliminated by making use of a curve plotted from real image characteristics by averaging brightness over all azimuth lines in each range column.

Either approach to trend elimination has the disadvantage of sensitivity to wind speed variance over the image field. In other words, large variations in the wind speed across the image field lead to equally large variations of σ^0. As a result, this method of trend correction is unsuitable under certain conditions.

Enhancement of contrast in radar images is indispensable for their interpretation. As a rule, this operation is performed in conjunction with an image smoothing procedure (low-frequency filtration) for which the windows with 3×3, 5×5 or another number of pixels are employed.

Whenever the observed phenomena need to be exactly located at the underlying surface, RI are transformed into the geographic projection in the program environment of a relevant geographic information system, such as ERDAS Imagine, ENVI, ARCInfo, etc.

Periodic and quasi-periodic structures are studied using spectral methods of image processing that allow wave processes to be described both at the surface and in the depths of the ocean. The possibilities of employing spectral analysis of surface wave fields were investigated in Refs [14, 15]. Spectral processing permits the study not only of the surface waves proper but also of meso- and macroscale phenomena (currents, fronts) that tend to distort surface wave fields under certain conditions (see Ref. [16]).

A typical procedure for spectral processing of image fragments includes the following main stages:

(1) Subtraction of mesoscale variations produced by wind field nonuniformity, slicks, etc. from the radar image. To achieve this, the original image is first subjected to low-frequency filtration. Then the original image is divided into the filtered image in the element-by-element manner. In this way, large-scale fluctuations (e.g., over 1000 m in size) are eliminated, and only surface waves remain to be analyzed.

(2) Fast complex Fourier transformation of the image obtained.

(3) Calculation of the modulus squared of the complex values.

(4) Smoothing the image obtained by a 15×15-pixel window.

(5) Normalization of impulse response with respect to the stationary function in order to weaken effects of sea surface movements.

Such methods have been developed, for example, at the Institut für Meerskünde, Universität Hamburg, Germany [17].

3. Mechanisms of microwave scattering from the sea surface

3.1 Two-scale model of the surface

In the microwave range, water is a conducting fluid with dielectric constant

$$\varepsilon = \varepsilon' + \mathrm{i}\varepsilon'' , \tag{2}$$

the real and imaginary parts of which are frequency-dependent [8]. ε' and ε'' values are comparable, for example, $\varepsilon = 49.3 + \mathrm{i}\,39.5$ at a wavelength of $\lambda = 3$ cm [18]. Bearing in mind relatively high values of ε' and ε'', water may be regarded in the first approximation as an ideal conductor.

ε' and ε'' show weak temperature and salinity dependence which accounts for the fact that a radar scattering cross section is first and foremost determined by the surface shape and to a much smaller extent by other factors.

A sea-surface wave spectrum is usually divided into large- and small-scale portions. The former encompasses waves longer than 1 m, while the latter includes gravity-capillary waves with centimeter lengths and partly decimeter waves ('ripples', as they are called). The *two-scale* or *composite* model is also qualified as 'ripples on a large wave'. Effects of ripples are described by the perturbation theory (Bragg scattering mechanism), and those of the large-scale component by the series expansion in small slopes of the surface [19–24]. Therefore, the small-scale component of sea-surface waves (its 'centimeter' fraction) proves to be responsible for the radar backscattering, while the large-scale one is responsible for the spatial modulation of scattered signals. The two-scale model of surface waves adequately describes scattering at large angles but needs to be improved when applied to the description of low-grazing-angle microwave backscattering. Some recent data on this subject are discussed in Section 3.3.

3.2 Resonant (Bragg) scattering mechanism

The universally accepted *resonance theory* of microwave scattering is based on the perturbation method. In the framework of this method, the height $z = \zeta(\boldsymbol{\rho})$ of surface roughness is considered to be small compared with the wavelength λ of an electromagnetic wave: $|z| \ll \lambda$; hence the appearance of a small parameter $\mu = k\sigma_\zeta \ll 1$ in the Maxwell equations [here, $\boldsymbol{\rho} = (x, y)$ — two-dimensional vector in plane x, y, and $\sigma_\xi = \langle \zeta^2 \rangle^{1/2}$ — root-mean-square surface perturbation]. Wave field $\mathbf{E} = \mathbf{E}_{\mathrm{inc}} + \mathbf{E}_{\mathrm{s}}$ is the sum of incident ($\mathbf{E}_{\mathrm{inc}}$) and scattered ($\mathbf{E}_{\mathrm{s}}$) waves; it can be naturally expanded in a power series of μ using the condition of orthogonality of the total field $\mathbf{E}$ and the boundary of a highly-conducting fluid. The intensity of the leading term of the series (single-scattering approximation) is convenient to characterize by the normalized scattering cross section σ which is a dimensionless quantity (the scattering cross section in square meters refers here to a unit area).

A simplified expression for the normalized scattering cross section and horizontal polarization of the radar signal has the form [22, 24]

$$\sigma_{\mathrm{h}}^{\mathrm{res}} = 4k^4 (\cos\theta)^4 \, F_\zeta(\mathbf{q}) , \tag{3}$$

where θ is the angle of incidence with respect to the vertical. Quantity $F_\zeta(\mathbf{q})$ is the spectral density of surface roughnesses and is related by the Fourier transform

$$F_\zeta(\mathbf{q}) = \frac{1}{4\pi^2} \int K_\zeta(\boldsymbol{\rho}) \exp(\mathrm{i}\mathbf{q}\boldsymbol{\rho}) \, \mathrm{d}\boldsymbol{\rho} \tag{4}$$

to the correlation function of surface roughnesses

$$K_\zeta(\boldsymbol{\rho}) = \left\langle \zeta(\boldsymbol{\rho}' + \boldsymbol{\rho}) \, \zeta(\boldsymbol{\rho}') \right\rangle . \tag{5}$$

Here, $\mathbf{q}$ denotes the horizontal component (in the x, y plane) of a scattering vector $\mathbf{k}_{\mathrm{s}} - \mathbf{k}_0$ that equals the difference between the scattered wave vector $\mathbf{k}_{\mathrm{s}}$ and the primary wave vector $\mathbf{k}_0$. In the case of a strict back scattering, when $\mathbf{k}_{\mathrm{s}} = -\mathbf{k}_0$, we have $\mathbf{q} = 2\mathbf{k}_{0\perp}$ ($\mathbf{k}_{0\perp}$ is the horizontal component of vector $\mathbf{k}_0$). Hence, for the absolute value of q, one finds

$$q = 2k \, \sin\theta . \tag{6}$$

Quantity q corresponds to the spatial harmonic of surface perturbation $\Lambda = 2\pi/q$. Due to formula (6), this harmonic is related to the electromagnetic wavelength $\lambda = 2\pi/k$ by the formula

$$\Lambda = \frac{\lambda}{2 \sin\theta} , \tag{7}$$

known as the Bragg equation. This equation gives the resonant wavelength of perturbation that selectively transforms the primary wave incident at an angle θ to a scattered wave running in the reverse direction. According to Eqn (7), in the case of grazing incidence (when the incident wave vector makes a small angle $\gamma = \pi/2 - \theta$ with the fluid surface), the resonant water wavelength Λ is $\lambda/2$ but increases infinitely with approaching the nadir ($\theta \to 0$): $\Lambda = \lambda/(2 \sin\theta) \to \infty$.

In accordance with Eqn (3), the scattering cross section for the case of horizontal signal polarization and grazing observation angles $\theta \to \pi/2$ (or when $\gamma = \pi/2 - \theta \to 0$) tends to zero as $(\cos\theta)^4 = (\sin\gamma)^4$. A different situation occurs for the vertical polarization:

$$\sigma_{\mathrm{v}}^{\mathrm{res}} \approx 4k^4 f(\theta) \, F_\zeta(\mathbf{q}) , \tag{8}$$

where $f(\theta) \approx 1$ is an almost constant formfactor [22, 24].

Wind is the main cause of ripples (short gravity-capillary waves at the sea surface). It follows from Eqns (3) and (8) that the intensity I_{s} of the signals scattered from the water surface and received by the scatterometer antenna is proportional to the spectral density of small-scale perturbations $F_\zeta(\mathbf{q})$ which in turn depends on wind velocity V. Simultaneous measurement of I_{s} on board satellite and wind velocity V near the ocean surface provides data for the construction of the gauge dependence $I_{\mathrm{s}} = f(V)$. Such a dependence may be used to derive the wind velocity V from I_{s} values obtained by satellite radars to an accuracy of approximately 2 m s^{-1} [25].

Various structures at the ocean surface are made visible due to different mechanisms of ripple modulation, in the first place due to currents and surface-active substances (SAS) that cause the surface tension to change. Some of these modulation mechanisms will be considered below in Sections 4 – 8.

3.3 Evidence for the existence of nonresonant scattering mechanisms

The majority of phenomena observable by radar sensing of the ocean surface can be explained in the framework of the resonant scattering mechanism. At the same time, a wealth of data suggests the existence of nonresonant mechanisms of scattering.

Experiments at low grazing angles have demonstrated that, besides ripples, breaking waves make important contribution to radar signal scattering by the sea surface [26, 27]. Sometimes, for horizontal signal polarization, the spiking events are observed with an amplitude 10 – 15 dB higher than the mean level of radar scattering from the ripples.

Such radar signal spikes are, naturally, ascribed to the breaking of large surface waves, hereinafter referred to as *macrobreaking* events to differentiate them from the microbreaking of mesoscale water waves dealt with in Section 3.4. The breaking of large waves is a complex dynamic process and a focus of many current investigations (see, for instance, Ref. [28]). Mechanisms that underlie this process in the open ocean and nearshore waters remain to be elucidated; at present, they are largely described in a statistical sense [29, 30]. Certain authors have studied the effects of various factors associated with wave breaking formation of radar signals. Diffraction of electromagnetic waves by sharp-crested surface waves was considered in Refs [31 – 34]. Papers [35, 36] are devoted to the radar backscattering from the wedgelike shapes of wave crests in the area of the hydraulic 'spilling breaker – surface wave' jump. Reference [37] concerns specular reflection of electromagnetic waves from surface wave crests during formation of a 'plunging' breaker.

A further non-Bragg mechanism of microwave scattering by two-phase media ('water droplets in the air' and 'air bubbles in water') was investigated in paper [38]. This study evaluated respective quantitative contributions of the above mechanisms to the backscattering cross section in the Ku-band depending on wind speed and the angle of incidence of electromagnetic waves.

The work of Trizna et al. [39] is concerned with the analysis of 'spikes' of horizontally polarized radar signals reflected from counterrunning waves at grazing angles. This paper describes the results of laboratory experiments using a dual-polarization X-band radar with high spatial resolution ($\approx$ 10 cm). Based on these results, the authors concluded that 'scatterers' should be located not on the crests of dominant surface waves but more likely at their rear slopes in the immediate proximity to the crests. It is inferred that such scatterers are actually crests of mesoscale waves (1 m in length or shorter) driven to extreme steepness close to the crests of longer waves [39]. The authors of Ref. [39] did not report a model computation enabling interpretation of their experimental results, but they claimed that the mechanism described is different from all those reviewed in preceding paragraphs.

Results of field experiments designed to study the relationship between the microwave backscattering cross section and the grazing angle can also be found in Ref. [40] where it is suggested that mesoscale wave breaking should be regarded as a scatterer responsible for the radar signal spikes.

Other publications also take into consideration sharpening and breaking of mesoscale waves [41 – 43] superimposed on macrobreaking events, i.e., breaking of large nearshore waves.

Kropfli and Clifford [44] presented radar data acquired when experimenting at grazing angles in a wavelength range from 8 to 12 cm. The authors showed that sensing against the wind and waves revealed identical scattering cross sections for vertical and horizontal polarizations of radar signals, whereas sensing in the opposite direction (downwind) yielded σ^0_{VV} values 8 – 10 dB higher in the average than σ^0_{HH}. Concurrent Doppler downwind measurements of the speed demonstrated the identity of the results for horizontal and vertical polarizations, while upwind sensing showed that speeds corresponding to the Doppler frequency shift for horizontally polarized signal were 0.5 – 1.0 m s^{-1} higher than that for the vertically polarized one. This somewhat unexpected finding cannot be explained unless the scatterers contributing to σ^0_{HH} and σ^0_{VV} are assumed to be spaced at a certain interval. The observed phenomenon is interesting in that it characterizes the mean scattering power rather than 'spikes'.

To summarize, a large amount of evidence is available today in support of nonresonant (non-Bragg) mechanisms of electromagnetic scattering. Putting aside the most expressed manifestation of nonresonant scattering, i.e., scattering of radar signals from macrobreakings, it may be argued that the effects of nonresonant mechanisms are most apparent at grazing angles. They are listed below.

(1) *Radar backscatter spikes for horizontally polarized signals*. Kalmykov and Pustovoytenko [31] were among the first authors to put forward the hypothesis of nonresonant (non-Bragg) microwave scattering at low grazing angles. They described spikes of backscattered signals (mostly with horizontal polarization) recorded in observations against the motion of sharpened waves. Similar spiking events were reported by many later authors [32 – 34, 45, 46].

(2) *Angular dependence of radar cross section for two polarizations*. Limitations of the traditional two-scale model as applied to observations at grazing angles have been convincingly demonstrated in Ref. [47] concerning angular dependence of a radar cross section for vertical and horizontal signal polarizations. According to Guinard et al. [47], the intensity of radar signals for the case of horizontal polarization when $\gamma \to 0$ does not tend to zero as quickly as predicted by the resonance theory [see formula (3)]. The difference between Bragg theoretical and observed values can reach 10 – 20 dB.

(3) *Doppler spectra taken at two polarizations*. The third piece of evidence in proof of nonresonant effects is the peculiarities of Doppler spectra of backscattered signals received at two signal polarizations. It has been shown in experiment by Lee et al. [45, 46] that the Doppler shift for vertical polarization at a grazing angle of observation is in excellent agreement with the Bragg theory's prediction. Conversely, the Doppler shift for horizontal polarization is much greater than the theoretical one related to resonance scattering and corresponds to the phase velocity of sea waves about 1 m long.

(4) *Dual-polarization images of the ocean obtained at grazing angles*. The fourth and most convincing piece of evidence of the nonresonant mechanism is provided by dual-polarization observations of the ocean under stable and unstable conditions of atmospheric stratification. Demon-

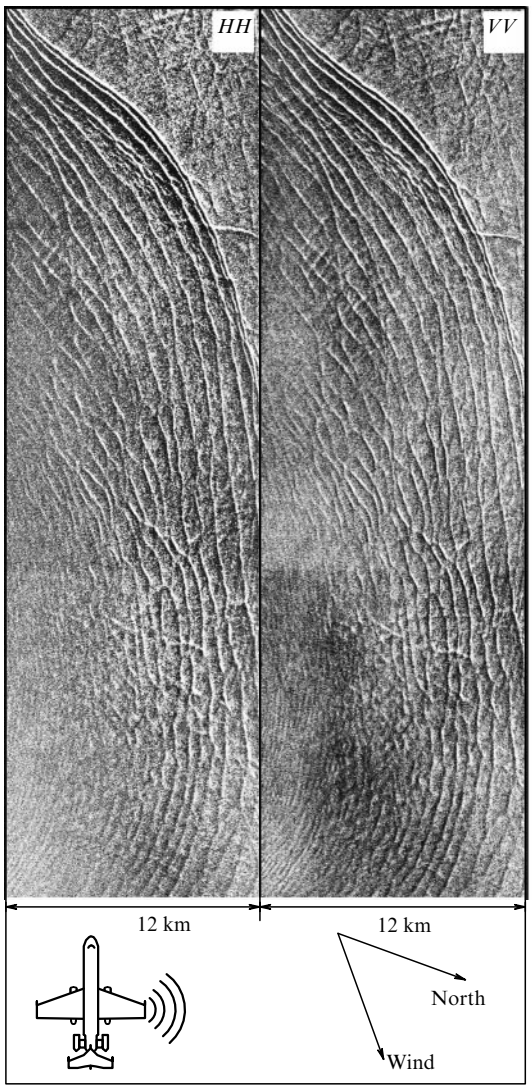

Figure 2. Images of an ocean area, obtained by the airborne Nit' dual-polarization radar station at stable atmospheric stratification: left — horizontal polarization, right — vertical polarization.

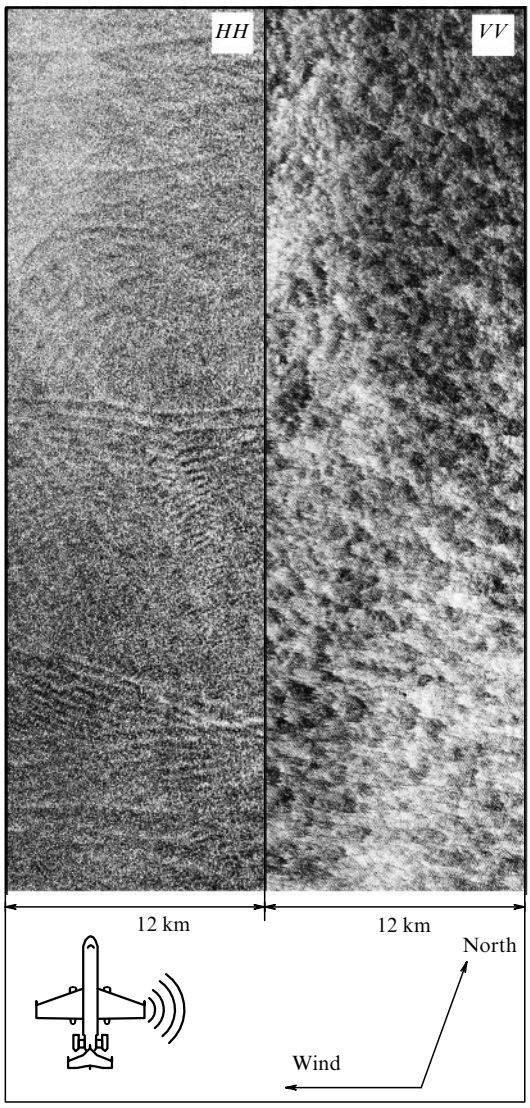

Figure 3. Images of an ocean area, obtained by the airborne Nit' dual-polarization radar station at unstable atmospheric stratification: left — horizontal polarization, right — vertical polarization.

strative examples of the resulting radar images are presented in Figs 2 and 3 [48].

These images were obtained by a Nit' radar station aboard the TU-134 aircraft-laboratory. The radar allowed internal waves with a spatial period of about 1 km to be observed within a surveillance strip of about 12 km in width. Images of the ocean obtained for two signal polarizations at stable air stratification proved very similar (Fig. 2), thus suggesting for the most part a single mechanism behind their formation. A radar image taken for vertical polarization of signals under unstable atmospheric stratification, when water temperature is higher than air temperature, looks different from that for horizontal polarization (Fig. 3). In these conditions, convective cells about 1–2 km in diameter are known to develop in the atmosphere. These cells exhibit inhomogeneities in the wind field that cause ripples in the places where the nearsurface wind velocity is high. Such ripples are fairly well apparent for vertical polarization of signals, whereas effects of convective cells for horizontal polarization are virtually absent.

The resonance theory offers expressions (3) and (8) for microwave scattering cross sections in the case of horizontal and vertical signal polarizations, respectively. The two expressions differ only in coefficients of spectral density $F_\zeta(\mathbf{q})$. It follows from the proportionality of σ_h and σ_v to one and the same quantity $F_\zeta(\mathbf{q})$ that images must be similar for horizontal and vertical polarizations (as seen in Fig. 2). The observed discrepancy between the two images of the ocean, obtained under different air stratification conditions (Fig. 3), provides unambiguous evidence of a scattering mechanism different from the resonant one. It will be considered in the next section.

3.4 Nonresonant mechanism of scattering from steep breaking waves. Three-component model of the surface

Analysis of the set of data undertaken in papers [49–54] has shown that the most probable source of nonresonant scattering is steep and short *mesoscale* waves about to break up. Their characteristic lengths (50–100 cm) and heights (10–20 cm) are intermediate between those of small-scale (a

few centimeters) and large-scale (meters and longer) components of the surface wave spectrum. The inclusion of mesoscale waves in the two-scale model of the sea surface turns it into a *three-scale* model. In fact, the aim of this procedure is not so much to add intermediate spatial scales to the two-component model, as to introduce waves of a new quality, namely, steep short waves about to break up. The origin of such waves remains an open question, even though their existence is generally recognized.

In what follows, we consider the scattering of electromagnetic waves based on a model of steep mesoscale breaking waves whose two-dimensional profile is depicted in Fig. 4. The figure shows four scattering channels for an incident electromagnetic wave that result in its return to the radar transceiver antenna. First, the radar signal is reflected backward directly from a wave edge. Second, there is a scattering channel where the electromagnetic radiation reflected from the sea wave edge (point C) undergoes secondary scattering from the sea surface at point F just forward of a breaking wave and only then travels back to the radar receiver. The third scattering channel is opposite to the previous one in terms of direction and is fully coherent with it. Fourth, there occurs triple reflection in which an incident signal is first reflected from the horizontal surface at the foot of the wave at point F, then goes back after reflection from the wave edge at point C, and is finally reflected once again from the sea surface at point F in front of the breaking wave.

The interference between these scattering channels may either increase the strength of the back scattered signal or decrease it. Such process accounts in part for a marked difference in the character of polarization-specific scattering from steep breaking waves. Another important cause of polarization-related differences at grazing angles of observation is the attenuation of a vertically polarized electromagnetic signal (compared with a horizontally polarized one) at the foot of a breaking wave. This effect is most pronounced when the grazing angle of incident radiation is close to the Brewster angle reported to be approximately 7° for a wavelength of 3 cm at the water temperature 10 °C and salinity 35 ‰ [2]. Taken together, interference and Brewster's effect may be responsible for the strong reflections of the signal when operating at horizontal polarization ('super' events) described, for example, in Refs [45, 46]. These effects prevail at large observation angles. When the angles are close to the nadir, double reflections are unlikely, and the contribution from breaking waves becomes less apparent against resonant scattering which is more intense under these conditions.

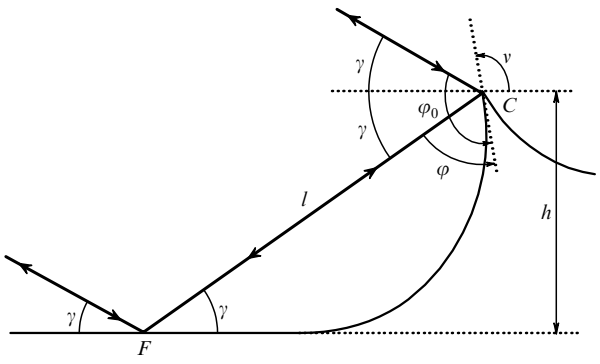

Figure 4. Interfering scattering channels in diffraction of electromagnetic waves by a steep mesoscale sea-surface wave.

Although nonresonant scattering at moderate observation angles is relatively less important than resonant scattering, its contribution to polarization-related effects remains significant because depolarization is largely due to the action of steep rather than sloping wavelets. This fact finds confirmation in Ref. [55], among other publications, which develops ideas that come close to ours even though the authors do not resort to the notion of nonresonant scattering. It is worthwhile to note that calculations of depolarization reported by Kudryavtsev et al. [55] compare qualitatively to the results of satellite observations.

Recently, steep waves and effects related to concave depressions at the long wave surfaces have attracted increased interest as evidenced by a number of relevant publications [56, 58]. By way of example, Voronovich and Zavorotny [56] arrived at good agreement with experimental data based on the small tilt approximation. Multiple reflection and the related multiple scattering from small roughnesses in concave areas at the sea surface were described in Refs [57, 58].

The authors of works [49 – 52] proposed analytical expressions for backscattering cross sections in the frames of breaking wave model presented in Fig. 4. The electromagnetic field scattered by a sharp-crested breaking wave was calculated by the methods of the geometrical theory of diffraction [53]. According to paper [51], cross sections of back scattering from a single breaking wave for two orthogonal polarizations of the signal have the form

$$\sigma_{\mathrm{h,v}} = \frac{2\pi L^2}{\sqrt{1+4k^2h^2\sin^2\gamma}}\,|D_{\mathrm{h,v}}|^2 \times \exp\left(-\frac{4L^2k^2\cos^2\gamma\sin^2\varphi}{1+4k^2h^2\sin^2\gamma}\right). \quad (9)$$

Here, L is the effective length of the breaking wave crest, h is the wave height, and φ is the angle between the steep wave direction and the reflected signal direction (the case of $\varphi = 0$ corresponds to the breaking wave motion exactly towards the observer).

Polarization characteristics of backscattering cross sections are determined by diffraction coefficients $D_{\mathrm{h,v}}$. The squares of the modules of these coefficients depend on a variety of parameters as illustrated by Figs 5a – d where solid and dashed lines show values for vertical and horizontal signal polarizations, respectively. In all the figures, the exterior vertex angle of the wedge tangent to a breaking wave is taken to be $\alpha = 270°$. For the purpose of computation, it was assumed that the incident radiation wavelength is $\lambda = 3$ cm and the radius of curvature of the sea wave forefront a_{f} satisfies the condition $ka_{\mathrm{f}} = 20$.

Figure 5a is a plot of $|D_{\mathrm{h,v}}|^2$ versus the steep wave height taken to be $h = l\sin\gamma$, where l is the distance between the two reflection points (see Fig. 4). The oscillatory character of $|D_{\mathrm{h,v}}|^2$ dependence on h is due to the interference of different scattering channels shown in Fig. 4. The vertically polarized signal is much weaker than the horizontally polarized one, because the Brewster effect at the selected grazing angle (around 7°) tends to significantly weaken all scattering channels except the straight one. This effect (although for large breaking waves) was predicted in Refs [39, 40].

Figure 5b presents a plot of $|D_{\mathrm{h,v}}|^2$ versus the tilt angle v of the breaking wave forefront relative to the horizontal surface.

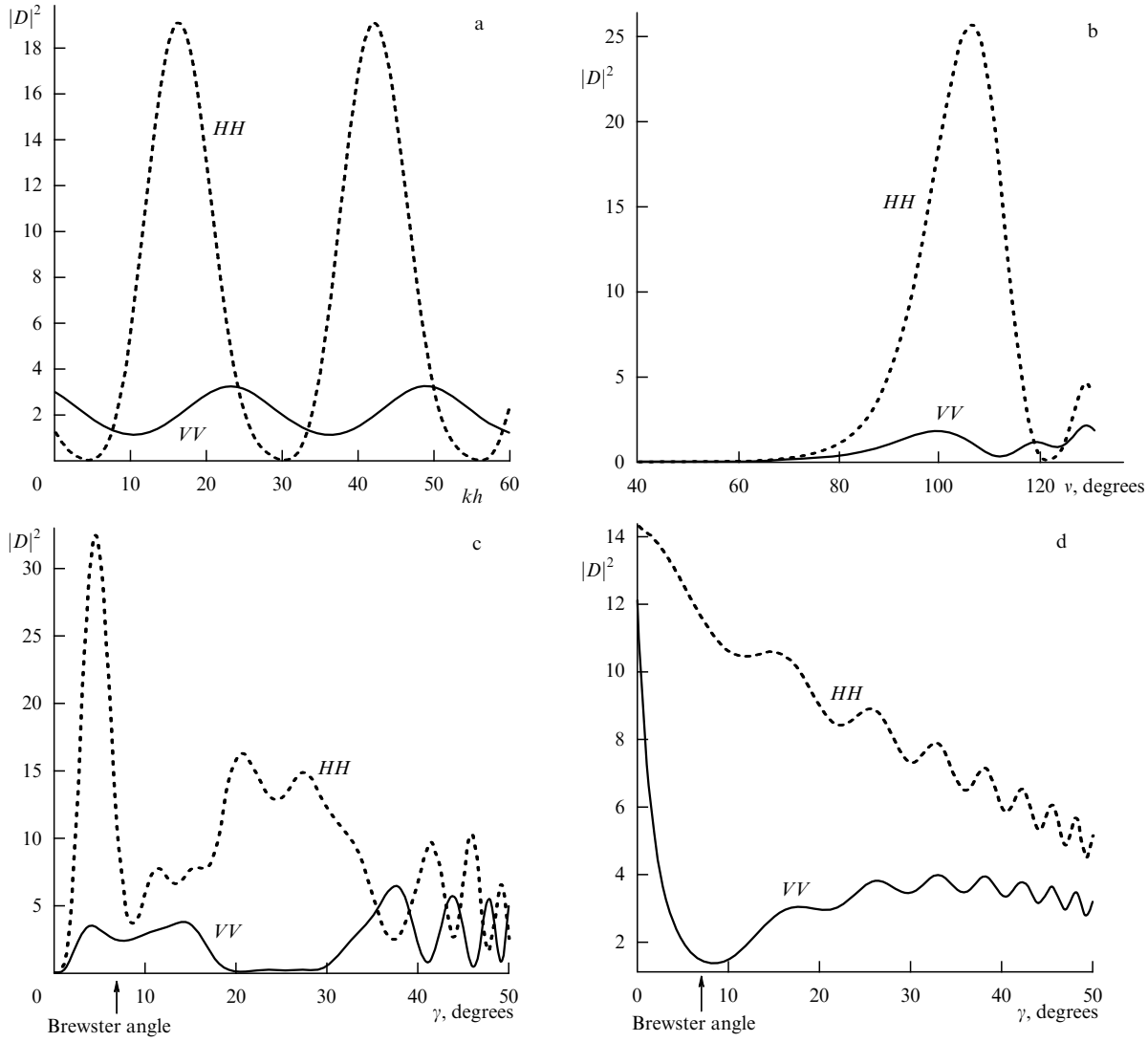

Figure 5. The squares of modules of diffraction coefficients for vertical ($|D_v|^2$ – solid lines *VV*) and horizontal ($|D_h|^2$ — dashed lines *HH*) polarizations plotted against: dimensionless wave height kh at $v = 100°$, $\gamma = 7°$ (a); tilt angle v of wave at $\gamma = 7°$, $kh = 16$ (b), and grazing angle γ at $v = 110°$, $kh = 25$ (c). Plots of $|D_{h,v}|^2$ averaged over wave height vs. grazing angle γ at $v = 110°$ (d) are also presented. In all cases, the exterior angle of wedge opening is assumed to be $\alpha = 270°$, wavelength of incident radiation $\lambda = 3$ cm, and radius of curvature of the wave forefront a_f is such that $ka_f = 20$.

The figure shows that the backscattering cross section reaches a maximum after the wave crest begins to spill down as the forefront inclination becomes greater than 90°. Because the vertically polarized component loses part of its strength upon reflection from the wave base, scattering intensity for vertical signal polarization is again lower than for horizontal polarization.

Finally, Fig. 5c shows the dependence of $|D_{h,v}|^2$ on the grazing angle γ of an incident wave. It can be seen that the curves corresponding to vertical and horizontal signal polarizations are in antiphase at grazing angles higher than the Brewster angle of 7°. This can be accounted for by the fact that, at sufficiently large grazing angles, the horizontally polarized component undergoes an additional phase shift of 180° as it is reflected from the wave base. For this reason, the condition of the appearance of maxima for one polarization should be in line with the condition of the appearance of minima for the other polarization. Due to suppression of the vertically polarized component in the vicinity of the Brewster angle of incidence, scattering pertaining to horizontal polarization of the radar signal is much stronger than that to vertical polarization (see Fig. 5c). Also, it follows from Fig. 5c that interference may have an even greater influence on polarization characteristics than the Brewster effect, for example, over a range of grazing angles from 25° to 40°.

When the resolution element is sufficiently small and the area visualized by the radar experiences on average less than one electromagnetic wave reflection, the back scattered signal has the form of a sharp spike with an amplitude defined by formula (9). For the remaining time, the signal being received is rather weak (at grazing angles of observation). However, if multiple wave breaking events occur within the radar sensing area, the backscattering cross section (9) should be averaged over all possible shapes, sizes, and directions of the breaking waves.

Assuming that wave crest orientations approximate Gaussian distribution with the root-mean-square deviation φ_0, the averaged backscattering cross section is defined by the expression [51]

$$\langle \sigma_{h,v} \rangle = \frac{n\lambda L}{2\varphi_0 \cos\gamma} \langle |D_{h,v}(\alpha, v)|^2 \rangle_{\alpha,v,h} \exp\left(-\frac{\Delta\varphi^2}{\varphi_0^2} \right), \quad (10)$$

where n denotes the number of breaking events that occur each moment within a unit area, $\Delta\varphi$ is the angle between the average direction of steep wave lines and the direction of propagation of backscattered radiation, and the angle brackets indicate averaging over the exterior angle of wedge opening α, tilt angle of wave front v, and wave height h.

Averaging over the wave height h results in a marked smoothing of the interference between different scattering channels because it is the wave height that regulates their phases. This accounts for smoothed interference oscillations in the plots of averaged $|D_{\mathrm{h,v}}|^2$ values versus the grazing angle (see Fig. 5d) and the clearly seen attenuation of the vertically polarized signal at grazing angles approximating 7°, i.e., the Brewster angle.

The density n of breaking events needs to be evaluated for explaining experimental data. It follows from Fig. 5c that the mean square of the module of the diffraction coefficient $|D_{\mathrm{h,v}}|^2$ is on the order of 5 for breaking waves with $a_{\mathrm{f}} \approx 10$ cm and $h \approx 8$ cm at a grazing angle of 7°. If $\lambda = 3$ cm, $L = 1$ cm, and $\varphi_0 = 0.1$ rad, then the back scattering for horizontal polarization is $\langle\sigma_{\mathrm{h}}\rangle \approx 0.75n$, in accordance with Eqn (1). It was found in experiment [47] that the mean backscattering cross section is -35 dB for horizontal polarization of the radar signal at grazing angles. Hence, breaking wave density $n \approx 4 \times 10^{-4}$ m^{-2} (i.e., one breaking event per 2500 m^2) is sufficient to account for the observed scattering cross section, provided all these waves travel towards the observer.

Figure 6 shows sea surface images obtained using a mobile dual-polarization radar equipped with a digital data processor in an experimental investigation conducted by the Space Research Institute, RAS on the Black Sea in 2000 (based on the Southern Division of the Institute of Oceanology, RAS at the Gelendzhik) [54]. The radar afforded a high resolution (around 15 m in range and azimuth) which justified the interpretation of individual light spots on the radar images as reflections from solitary steep waves (Bragg scattering would have produced uniformly greyish images). This enabled the use of the images for counting solitary steep waves per unit area. It was estimated at 4×10^{-4} m^{-2} for horizontal and $(5-6) \times 10^{-4}$ m^{-2} for vertical signal polarizations. Interestingly, light spots for the case of horizontal polarization showed up with stronger contrast than for the vertical polarization, but their number was somewhat smaller.

Taken together, these images and those presented in Refs [40, 42] suggest the existence of steep mesoscale waves at the sea surface.

In summary, the modern theory of electromagnetic wave scattering from rough surfaces is based on a combination of two approaches. One is the perturbation method dealing with small disturbances whose height is generally low compared with the length of electromagnetic waves (resonant or Bragg scattering). The other is the Kirchhoff approximation applicable to high gently-sloping disturbances having a height much greater than the radar sensing wavelength. This combined approach is known as the two-scale scattering model. Nevertheless, the standard two-scale model does not describe nonresonant scattering by steep breaking waves. On the one hand, they are too high compared with electromagnetic wavelengths and allow no application of the perturbation method. On the other hand, their steepness precludes application of the Kirchhoff approximation.

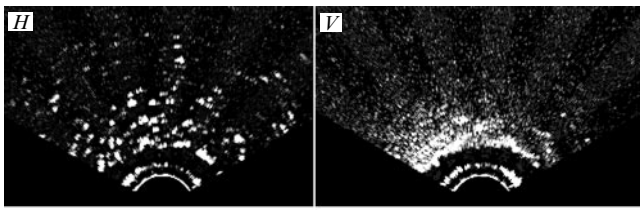

Figure 6. Sea-surface radar images obtained by an X-band radar at grazing angles of 1 – 4° with the horizon. Left: horizontal polarization, and right: vertical polarization. Each image covers an area of 1.4×2.2 km^2.

An adequate description of back scattering, especially at grazing angles and for horizontal polarization of sensing radiation, requires that the breaking of high and steep sea-surface waves be taken into consideration. Collectively, fulfillment of this requirement for steep breaking mesoscale waves and application of the standard two-scale model give rise to a three-component model of the wave-driven surface. Its novelty as compared with the universally accepted two-scale model consists not so much in the simple addition of one more scale as in its consideration of the contribution from steep breaking waves (10 – 20 cm high and about 1 m long) intermediate between Bragg waves with centimeter wavelengths and long (10 m and more) gravity waves of the energy-carrying part of the sea-surface wave spectrum. The introduction of this component radically changes scattered field characteristics at grazing angles and opens the way to the uniform description of scattering of both short (a few centimeters) and long (decimeters) sensing electromagnetic waves.

3.5 Other nonresonant scattering mechanisms

Experimental findings suggest diverse mechanisms involved in effects exerted by an aqueous medium on surface roughness, hence on observed contrast properties of radar images. One of these findings is an image of Lake Onega obtained by the Cosmos 1870 satellite under windless conditions in the summer 1989 [59]. The image shows a stronger signal area having clear-cut boundaries, the appearance of which cannot be explained in the framework of traditional concepts. Comparative analysis of ground-based, aircraft, and spacecraft observations revealed the following picture.

Part of the lake sensed by SAR exhibits an area of high phytoplankton concentration created by favorable weather conditions and unusual water circulation. The presence of phytoplankton is confirmed by visual observations and analysis of the transparency distribution in depth. Dying planktonic organisms release large amounts of gas bubbles that concentrate in the top water layer. This increases surface roughness (in the absence of wind) and thereby amplifies the radar returned signal. Nonuniform reflectivity in the western part of the area sensed by the radar is due to the wind-driven surface waves as confirmed by ship-borne observations. Temperature and transparency distribution patterns here are significantly different from those in the eastern part of the radar-sensed area in terms of both absolute values and intermittency. These facts suggest that radar contrast of the water surface results not only from known physical processes in the atmosphere and water column (wind, currents, internal waves, temperature fronts, etc.) but also from hydrobiological processes. This and other nonresonant mechanisms acting in foam and bubbles to modulate radar signals [60] make an appreciable contribution to radio scattering at grazing angles.

4. Radar images of surface waves

Let us now consider the formation of radar images of the ocean taking into account both resonant and nonresonant effects. In the above discussion of electromagnetic wave scattering from micro- and mesoscale components of the surface waves, we bypassed the triple effect of the large-scale (long-wave) component on the scattering patterns.

To begin with, the long-wave component alters the viewing angle of wind-generated ripples, so that the angle θ in formula (4) will be modulated by large water waves.

Secondly, the ripple spectrum $F_\zeta(\mathbf{q})$ is affected by local currents induced by large water waves. The point here is that fluid particles involved in a wave process travel along elliptical trajectories and thus create currents on the fluid surface. These currents tend to *lengthen* and modify gravity-capillary waves spreading with the fluid flow but cause the wave packets to *squeeze* if the gravity-capillary waves run in the opposite direction. These effects can be described by the equation for conservation of wave action [61, 62] (we shall work with this equation in Section 6).

Thirdly, Refs [63, 64] demonstrated the development of a train of wind-independent gravity-capillary waves close to the crests of large water waves. In paper [63], they are referred to as 'bound' Bragg waves to distinguish them from 'free' Bragg waves, i.e., gravity-capillary waves produced by the wind.

Collectively, these three processes are responsible for modulating the ripple spectrum $F_\zeta(\mathbf{q})$ with a large wave and thus create a prerequisite for the 'manifestation' of the large-scale component of the surface waves in radar images.

Certainly, such a 'triple' modulation produces the above effect if large waves are longer than the resolution element in a given radar. At a resolution of $\Delta x \approx 30$ m, this condition is satisfied only for sufficiently long ripples, say, surface waves having length $\Lambda \geqslant 60-100$ m.

The intensity of surface wave manifestations in radar images, i.e. contrast, is given by

$$\beta = \frac{I_{\max} - I_{\min}}{I_{\max} + I_{\min}}\,, \tag{11}$$

and depends on the angle α between the viewing and wind directions.

Figure 7 displays a fragment of the SAR image obtained in the summer of 2001 and showing a Black Sea area near the city of Novorossiĭsk with readily distinguishable surface waves. The well-apparent manifestations of wind-driven surface waves are due to a prolonged storm with choppy winds of 20 m s^{-1}.

Comparative studies of radar scattering from the sea surface in different frequency bands are reported in papers [37, 38, 65, 66]. Their main results obtained at moderate viewing angles can be summarized in the following way.

(1) With upwind sounding, the backscattering cross section σ^0_{UW} is larger than σ^0_{DW} in the case of a downwind sounding, with the $\sigma^0_{\mathrm{UW}}/\sigma^0_{\mathrm{DW}}$ ratio for horizontal polarization being higher than for the vertical polarization.

(2) The backscattering cross section σ^0_{CW} obtained in crosswind sounding is smaller than the relevant quantity resulted from upwind or downwind sounding, and the $\sigma^0_{\mathrm{UW}}/\sigma^0_{\mathrm{CW}}$ ratio for vertical polarization is greater than for the horizontal polarization.

(3) The $\sigma^0_{\mathrm{UW}}/\sigma^0_{\mathrm{DW}}$ ratio grows with increasing wind speed and reaches a maximum at about 9 m s^{-1}.

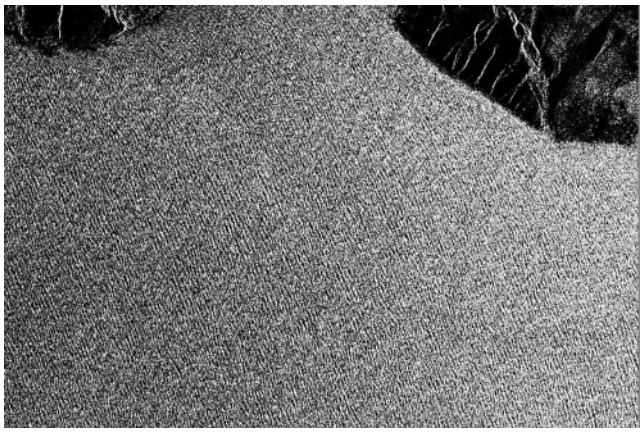

Figure 7. A fragment of SAR image of the Black Sea coastal area, obtained by the ERS-2 satellite on 6 June 2001 and showing wind-driven surface waves generated under storm conditions at the time of sensing.

(4) The ratios $\sigma^0_{\mathrm{UW}}/\sigma^0_{\mathrm{DW}}$ and $\sigma^0_{\mathrm{UW}}/\sigma^0_{\mathrm{CW}}$ grow with increasing the angle of incidence of an electromagnetic wave, at least in the resonant scattering region.

(5) For angles of incidence $\theta = 20^\circ - 70^\circ$, the azimuth-angle dependence of cross sections is fairly well approximated by the cosine function of the double angle.

The aforecited papers report relevant quantitative estimates of backscattering cross sections depending on the azimuth observation angle and wind velocity as well as sounding signal polarization, wavelength, and angle of incidence. For the near-downwind sounding in the short-wave (centimeter) range, the signal power is 3 – 10 dB higher than that for the crosswind sounding (depending on the wind velocity). The signal is strongest in the case of upwind sounding, where it is 2 – 3 dB higher than that obtained in downwind sounding at a constant wind velocity; there is practically no difference under gusty wind conditions.

5. Surface manifestations of internal atmospheric gravity waves and convective processes in the atmosphere

Internal gravity waves propagating through the stratified atmosphere are of different origin. Atmospheric wavelike disturbances can be generated by (among other things) air flow past terrain obstacles giving rise to the so-called internal lee waves [67], interactions between continental and oceanic air masses [68], and movements of atmospheric cold fronts described in Refs [69 – 71].

Internal gravity waves propagating in lower atmosphere are not necessarily associated with an accompanying cloud system and therefore are not always accessible to visual observations. Meteorological satellites of the GOES series [72] and NOAA satellites equipped with IR radiometers [73] provided optical images showing regularly arranged stripes of clouds presumably related to internal wave packets extending in the atmosphere.

Internal gravity waves traveling in the lower atmosphere used to be recorded in the past by a network of ground meteorological stations situated, for example, near Berlin, Germany [74 – 76] and in the central part of the USA [77]. These observations revealed trains of nonlinear waves that passed consecutively over different observing stations. Atmospheric wave processes were also identified in images obtained

by ground-based radar stations. These data are presented in papers [78 – 81].

Radar sensing of the ocean opens up new opportunities for the observation of atmospheric internal waves. Wave processes that occur in the atmosphere are manifested in radar images of the sea surface because the related variations of wind velocity and wind direction modulate surface roughness, hence modulated backscattering cross section. Gravity waves propagating in the atmosphere very close to the ocean surface were identified in radar sea-surface images presented in Refs [82 – 84].

A series of radar images taken simultaneously in the centimeter-wavelength range for two polarizations of the sensing signal were analyzed in paper [85]. The radar images presented in Fig. 8 show sea-surface disturbances caused by wind field fluctuations in the zone of enhanced atmospheric wave activity. The observed picture was interpreted in terms of the concept of internal waves generated by movements of atmospheric cold fronts. A train of internal waves immediately ahead of the front in motion has some properties of a train of solitons.

Wind velocity fluctuations are 'imprinted' on the sea surface and can be seen in radar images as spots of varying intensity brought about by centimeter ripples. In the beginning, this 'wind noise' was regarded as a factor interfering with the examination of surface waves and slicks formed by internal waves, currents, oil spills, precipitation, etc. [86, 87]. However, in the course of time it became clear that characteristics of this noise carry information about the spatio-temporal wind structure and therefore can be used to study atmospheric processes that occur close to the water surface. By way of example, Fig. 9 shows a fragment of the

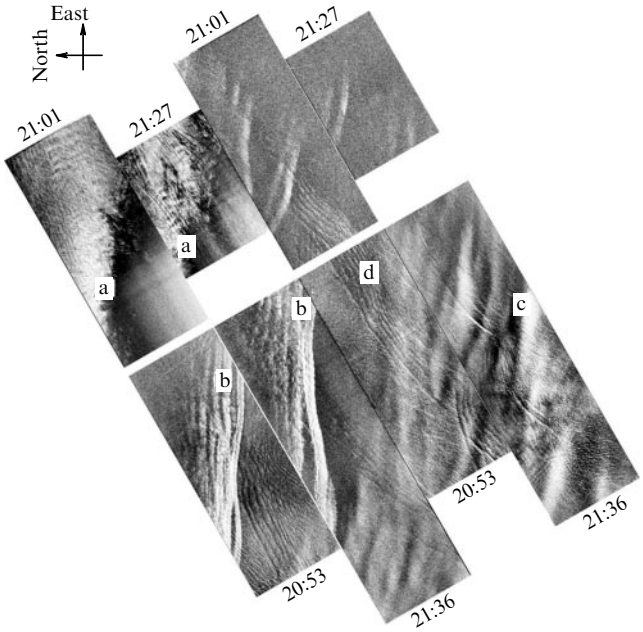

Figure 8. Radar sea-surface images (*VV* polarization) obtained on 15 July 1992. The abrupt change of the radio signal (a) occurs at the edge of the atmospheric cold front in motion. Quasi-periodic modulations of the radar signal (c) suggest the presence of a system of long plane atmospheric waves. Nonlinear, strongly contrast structures (b) are produced by a system of forced internal waves in the atmosphere, which are generated by a nonstationary convective process in its upper layers. Surface manifestations of tidal internal wave packets in the ocean are shown in (d).

Figure 9. Sea-surface radar image obtained with a vertically polarized signal and showing convective cells, offshore from Kamchatka, 28 August 1985. Wind velocity was 6 m s^{-1}; $T_{air} - T_{water} = -6.5\,^{\circ}C$.

radar sea-surface image obtained with a vertically polarized sensing signal of the Nit' SLAR just off the Kamchatka Peninsula in August 1985. The fragment contains imprints of convective structures.

The possibility to recognize and investigate convective processes in the near-water atmospheric layer using radar technology has been demonstrated in Refs [4, 88, 89]. These publications are based on the analysis of radar images taken in the three-centimeter wave range by orbiting spacecraft and showing convective circulations and eddies in the atmosphere. Convective rolls in the atmosphere above the sea surface were recorded in the Atlantic Ocean near Florida with the aid of a synthetic-aperture radar aboard a NASA aircraft [90]. Later, images containing similar structures were acquired by SAR mounted on the Seasat satellite [91] and by the space shuttle 'Columbia' in the SIR-A experiment [92]. All the above images represent only fully-developed and well-established atmospheric processes being free to modulate surface decimeter waves that serve as a

resonant component for radars operated in this wavelength range.

Manifestations of atmospheric effects on the ocean surface are also visible in images obtained by the ERS-1 satellite SAR (a wavelength of 5 cm) [93, 94].

Comparative analysis of radar images and atmospheric profiles obtained by radiosonde observations has led to the conclusion that there is the possibility to observe both wet and dry convections with the aid of radars operating in the centimeter wavelength range [6]. According to Ref. [6], the data acquired by radars can be used not only to establish the appearance of convection but also to characterize it in qualitative terms.

Such data were employed to determine the characteristic horizontal size of convective cells for both wet and dry convections that proved to be approximately 3 times their vertical size, the difference close to the theoretical value of 2.8 for the Rayleigh – Benard convection.

A theoretical model for computational analysis of radar images of the sea surface in the presence of atmospheric convective structures above the ocean under variable wind velocity conditions was suggested in paper [95]. The authors have done calculations for different frequencies (1.25, 5.30 and 9.6 GHz) and polarizations (*VV*, *HH*, and *HV*) of the sensing signal at moderate viewing angles and demonstrated good correlation between model predictions and remote sensing data obtained with the help of SIR-C/X-SAR radars aboard the space shuttle 'Endeavour' over the north-western portion of the Gulf Stream off the east coast of the USA.

6. Surface manifestations of internal waves in the ocean

Internal waves in the stably stratified ocean [96] are wavelike vibrations of water particles about a stable equilibrium position under the restoring action of Archimedes' (buoyancy) forces. In fact, such processes also occur at the air/water interface, only the difference between water densities deep in the ocean is almost one thousand times smaller than the difference between air and water densities. For this reason, the velocity of internal wave (IW) propagation is significantly lower, while their periods and lengths, as well as amplitudes of oscillations, are much greater than the respective parameters of surface waves. Unlike surface waves, internal waves entrain fluid particles that undergo vertical displacements with a maximum amplitude resided deep in the water rather than at the surface. At the same time, maximum amplitudes of horizontal displacements (orbital currents in IW) are found in the immediate proximity to the ocean surface where they reach almost 1 m s^{-1} and are responsible for marked changes in the small-scale wind waves spectrum.

This modulation can be quantitatively estimated using a kinematic model [51, 96, 97] based on the balance equation for wave action.

A theory based on the kinematic model was compared with the results of radar [51, 97] and microwave radiometric [98] measurements. It was concluded that the kinematic model fairly well explains the observed image contrasts if electromagnetic waves are relatively long (tens of centimeters and longer). However, for radars operating in the centimetric wave band, the observed values are one or two orders of magnitude higher than theoretical ones.

Two hypotheses were suggested to account for the marked contrasts observable in the range of centimeter waves. These are the cascade mechanism of modulation [51, 97] and the mechanism of modulation of the momentum flux towards the surface [99]. The former implies that the energy of short electromagnetic waves increases due to their interaction with short gravity waves undergoing strong modulation rather than with the flux gradient. The momentum flux modulation mechanism acts via restructuring turbulence of the near-surface layer promoted by the velocity gradient of the underlying surface.

There is one more approach to the explanation of surface manifestations of internal waves and topographical inhomogeneities of the undersea relief. The effects of these factors are especially apparent in nearshore areas under light wind conditions. The stationary solution of SAS modulation for a soliton-type internal wave has a concentration maximum over a region of extreme vertical displacements of the pycnocline and has no regions where SAS levels are lower than the background one. Therefore, images must contain only lower-contrast areas, and it is difficult to account for a marked rise in the backscattering cross section by the sea. Hence, it is necessary to resort to applying the above two mechanisms.

The principal mechanism of modulation in the mesoscale wavelength range (~ 1 m) appears to be the action of the internal-wave-generated subsurface current on the surface waves. The most prominent changes occur here under conditions reminiscent of group synchronism, i.e. when interaction occurs between those components of the sea surface waves (with the surface and internal waves propagating in the same direction) whose group velocity c_g approximates the internal wave phase velocity c:

$$c_g + u - c = 0\,, \tag{12}$$

where u is the subsurface current velocity. For typical phase velocities of internal waves (~ 1 m s^{-1}), this condition is met by mesoscale surface waves.

O M Phillips [100] was the first to consider the effects of the surface wave blockade by a current and demonstrate singularity of the solution in the form of an infinitely growing surface wave amplitude upon approaching group synchronism conditions (12). The solution giving quantitative characteristics of the interaction in critical areas was obtained in Ref. [101] for a nonlinear surface wave model. Consideration of the amplitude and modulation dispersion of surface Stokes waves propagating in a nonuniformly moving medium leads to the following dispersion equation

$$\omega^2 = gk + k^4\varphi^2 + \left(u(\zeta) - c\right)^2 \frac{\varphi_{\zeta\zeta}}{\varphi}\,,$$

where φ, ω, and k are the velocity potential amplitude, frequency and wave number of the surface wave, respectively, and ζ is the horizontal component in the coordinate system co-moving with the internal wave. In a nonlinear case, the 'kinematics' of interaction describing the behavior of the functions of surface-wave frequency and wave number in a current is inseparable from its 'dynamics' given by the law of conservation of wave action.

Analysis of the complete system of modulation equations [101] allowed for the description of a large number of interaction effects observed in nature, such as:

— greatly enhanced influence of subsurface currents under conditions close to group synchronism and markedly amplified contrasts compared with those predicted by the linear modulation model;

— nonuniform modulation of surface waves along a periodic train of short internal waves;

— possibility of formation of both forerunners and traces of internal waves on the sea surface;

— existence of bound surface-wave packets traveling together with internal waves in the absence of noticeable wind waves. (In the case of group synchronism, energy thresholds for surface wave generation are minimal.)

Let us now turn back to the analysis of radar images presented in Fig. 2 (stable atmospheric stratification) and Fig. 3 (unstable atmospheric stratification). Despite the identity of radar images in Fig. 2, obtained for horizontal and vertical signal polarizations, and the possibility of their qualitative interpretation in terms of the resonant scattering theory, the quantitative consideration of the degree of modulation leads to the conclusion that the resonant mechanism alone is insufficient to account for the observed effects.

Sections shown in Fig. 10 give the most characteristic examples of the representation of internal waves and atmospheric convection for different polarizations of the sensing signal. Generalization of all such data yielded by numerous experiments performed at the Space Research Institute (Moscow) has demonstrated that, for atmospheric internal waves and convection, the signal strength varied from 0.3 to 1 dB for horizontal and from 2 to 4 dB for vertical polarizations. In contrast, amplitude variations of the radar signal scattered from surface manifestations of internal waves in the ocean increased to 2 – 7 dB for horizontal polarization, but did not exceed 1.5 dB for the case of vertical polarization [103].

Another reason for the necessity of considering additional sources of scattering is provided by the results of statistical analysis of radar images of internal waves that propagate in the ocean in the plane of observation. In this case, radar image contrasts for vertical polarization under unstable stratification of atmospheric boundary layer are more pronounced than for stable stratification [104]. The difference between radar image contrasts at the two polarizations is illustrated by two branches of the curve in Fig. 11. One corresponds to stable (squares) and the other to unstable (circles) stratification of the atmospheric boundary layer. In addition, Fig. 11 presents data obtained at nearly neutral stratification of the boundary layer (triangles) in the presence of strong internal waves in the atmosphere. Under conditions of unstable stratification of an atmospheric boundary layer, radar images of internal waves in the ocean, taken for vertical polarization, prove to be obscured by variable near-surface winds.

The images in Figs 2 and 3 were acquired by means of radiation that hit the surface at grazing angle, i.e., when the scattering angle γ varied from 6° to 15°. It is in these conditions that the nonresonant mechanism of electromagnetic wave scattering from steep waves is triggered (see Section 3.4). Such steep short waves 10 – 20 cm in height serve as reflectors that reflect the incident wave back to the receiver. As a result, the complete scattering cross section is a sum of two components, one resonant and one nonresonant:

$$\sigma_{\rm v} = \sigma_{\rm v}^{\rm res} + \sigma_{\rm v}^{\rm nonres}\,,$$
$$\sigma_{\rm h} = \sigma_{\rm h}^{\rm res} + \sigma_{\rm h}^{\rm nonres}\,. \qquad (13)$$

It may be concluded from the comparison of Figs 10a and 10b [105] that, under unstable stratification of the atmospheric boundary layer and vertical polarization of the sensing signal, the resonant component $\sigma_{\rm v}^{\rm res}$ representing effects of convective air motions predominates. The contribution from horizontal signal polarization at grazing angles is much smaller, i.e., $\sigma_{\rm h}^{\rm res} \ll \sigma_{\rm v}^{\rm res}$. As a result, horizontal polarization is dominated by the nonresonant term $\sigma_{\rm h}^{\rm nonres}$. Therefore, under unstable atmospheric stratification, a dual-polarization radar is able to distinguish between internal motions in the ocean (ocean internal waves), which are visible for horizontal polarization, and wind-induced convective motions in the atmosphere, which are recorded for vertical signal polarization.

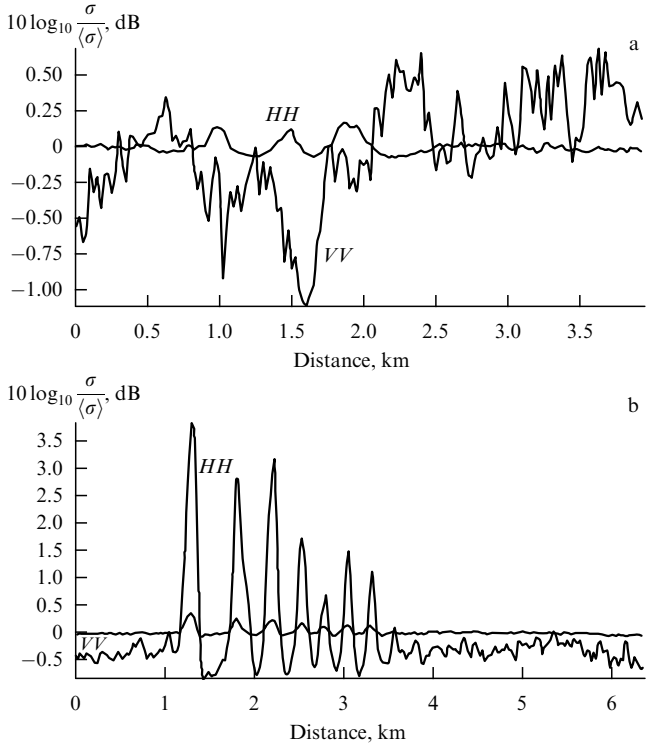

Figure 10. Intensity variation of a radar signal scattered from surface manifestations of convective cells in the near-water atmospheric layer (a) and from surface manifestations of internal waves in the ocean (b); *HH* — horizontal polarization, *VV* — vertical polarization.

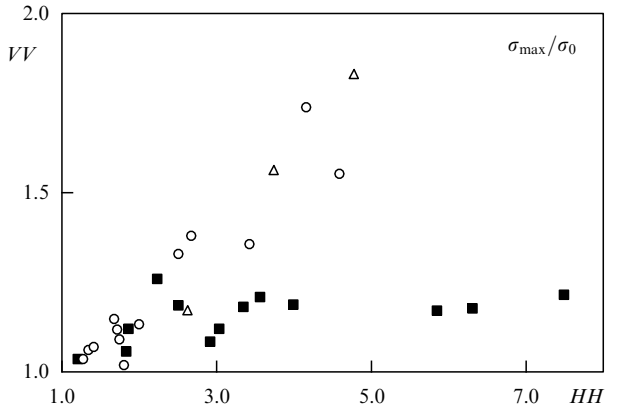

Figure 11. Relationship between radar image contrasts of surface manifestations of internal waves in the ocean for vertical and horizontal polarizations under stable (circles), unstable (squares), and neutral (triangles) stratification of the atmospheric boundary layer.

7. Currents, eddies, and hydrologic fronts

Currents, eddies, and hydrologic fronts can be seen in radar images in the first place because they modulate, in one way or another, surface wave spectra due to wave refraction by irregular currents, divergence and convergence of water flows, etc. Visualization of sea currents is also promoted by a number of other factors. To begin with, the interface between two currents is a place where various admixtures carried with water are 'sorted out'. These admixtures can make their own contribution to the scattering cross section that is not described by the resonance theory. Secondly, the wind interacts with a flowing fluid in a somewhat different manner than with a stationary one. Thirdly, strong currents (e.g., the Gulf Stream and some others) normally differ from the surrounding waters in terms of temperature and salinity. This accounts for a change in the surface tension of the water and ripple spectrum $F_\zeta(\mathbf{q})$. The first and third factors mentioned above also facilitate visualization of hydrologic fronts, i.e., interfaces between colder and warmer waters. Figure 12 presents images of a marginal area of the cold North Galapagos Current, which were obtained by the SIR C/X synthetic-aperture radar.

Papers [106–108] present interesting results of model computation of backscattering cross sections by hydrologic front boundaries. The experimental basis for these estimates was provided by the measurements made with the use of a side-looking airborne X-band radar (a wavelength of 3 cm) in a zone of strong convergence near a Gulf Stream boundary. Numerical models of radar signal intensity considered by Jansen et al. [106, 107] took into account interactions between short surface waves and currents generated by converging water flows but disregarded the effects of surface wave breaking. In both the cases, there is good qualitative agreement, whereas numerical evaluations of signal intensities at the edge of the hydrologic front turned to be much lower than the experimental values. It has been shown in Ref. [108] that consideration of the effects of surface wave breaking allows the quality of the model and correlation between theoretical calculations and results of radar experiments to be significantly improved. We believe it to be a weighty argument in support of the inference that not only the Bragg resonant mechanism but also breaking of steep surface waves in the convergence zone make an important contribution to electromagnetic wave scattering at the boundaries of hydrologic fronts and eddies.

A study of mesoscale eddies by Liu [109] using SAR images of the sea surface was based on numerical models taking into account wave/wind interactions, surface wave refraction, and effects of atmospheric instability. Also, it should be noted that Refs [110, 111] confirmed the possibility of applying remote sensing techniques to sounding the ocean surface and observation of vortical motions in the ocean and the air over it.

8. Surface-active substances and oil slicks

Both oil slicks and organic surface-active substances (SAS) are known to change surface tension and thereby 'smooth' sea roughnesses and decrease scattering cross sections. They are responsible for low-scattering areas at the ocean surface ('slicks') that may serve as indicators of surface pollution. By way of example, Fig. 13 presents a fragment of a SAR image of a Black Sea coastal area off the city of Novorossiĭsk. The radar image shows a well-apparent dark spot located 15–20 km from the shoreline. The dark color of the spot is due to the suppression of small-scale surface waves (thus, the intensity of backscattered radar signals) by an oil film resulting from the disposal of petroleum-contaminated water from a ship.

Automatic identification of oil slicks in radar images is not a simple task because at light wind in particular such slicks are difficult to distinguish from other objects and events generally referred to as their 'likeness'. Radar images bearing the likeness of oil slicks can be just as well produced by other organic films, some ice formations ('sludge'), areas shaded by shore structures, rain cells, and upwelling zones. Various types of oil-slick likenesses in RI have been considered in Ref. [112] which suggests a simple algorithm to be applied to discriminate between oil slicks and their likenesses.

Oil slicks and their likenesses in radar images have also been analyzed in papers [113–116]. As a rule, oil pollution of the sea surface produces dark spots in RI because oil films tend to damp ripples. Reference [113] reviews the ability of satellite-borne radars to reveal oil slicks. State-of-the-art approaches to radar sounding of oil slicks under different wind velocity conditions are discussed in work [116]. Wismann et al. [114] report the analysis of more than 150 oil slicks.

Naturally, radar images of oil spills depend on ambient conditions [115]. The contrast between an oil-covered area

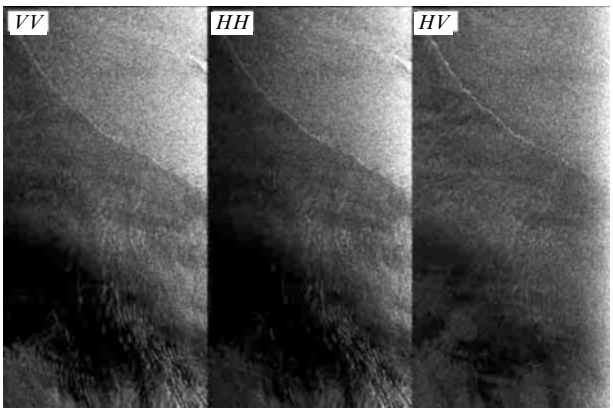

Figure 12. Radar images of the ocean surface over the North Galapagos Current obtained by an SIR C/X synthetic-aperture radar (L-band) on 4 April 1994 (by courtesy of R Romeiser and S Ufermann, University of Hamburg, Germany).

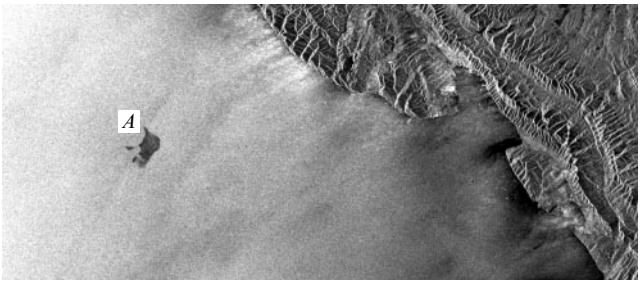

Figure 13. A fragment of an SAR image of a Black Sea nearshore area, obtained by the ERS-2 satellite on 26 July 1999. The dark spot marked by *A* is an oil slick.

and the surrounding water surface is determined by a number of environmental parameters, such as wind velocity, wave height, and the amount and type of spilled oil. The shape of oil spills differs depending on whether the oil was discharged from a moving or a stationary source; it is also a function of the amount of oil released into the water and of wind and current dynamics during the span of time that elapsed between the spill and the radar imaging.

9. Conclusion

The main objective of this review was to consider complicated physical processes responsible for the formation of radar images of the ocean, on the assumption that these processes are underlain by fundamental mechanisms described by Maxwell equations (as regards the electrodynamic aspect of the problem) and Navier – Stokes equations (hydrodynamic aspect). Actual manifestations of these mechanisms at the ocean surface can assume rather complex forms due to the effects of a variety of environmental factors, such as winds, currents, atmospheric and internal ocean waves, surface admixtures, SAS films, precipitation, to name but a few.

Strictly speaking, it is the multitude of factors that renders it difficult to interpret radar images of the ocean in the context of space oceanology. New physical (electrodynamic and hydrodynamic) models and computational techniques are indispensable for further progress in this important applied discipline.

In conclusion, the authors are grateful to the reviewers for responsive reading of the manuscript and valuable comments.

The work was supported by the Russian Foundation for Basic Research (grants 01-02-16174, 02-02-16012, 01-05-64464) and a few international projects (INTAS 99-0242 and CRDF RGI-2341-MO-02).

References

1. Lappo S S et al. *Issled. Zemli Kosmosa* (2) 70 (1997)
2. Raĭzer V Yu, Chernyĭ I V *Mikrovolnovaya Diagnostika Poverkhnostnogo Sloya Okeana* (Microwave Probing of the Ocean Surface Layer) (St. Petersburg: Gidrometeoizdat, 1994)
3. Kondrat'ev K Ya, Melent'ev V V, Nazarkin V A *Kosmicheskaya Distantsionnaya Indikatsiya Akvatoriĭ i Vodosbrosov* (Remote Sensing of Water Surfaces and Spillways from Outer Space) (St. Petersburg: Gidrometeoizdat, 1992)
4. Mitnik L M, Viktorov S V (Eds) *Radiolokatsiya Poverkhnosti Zemli iz Kosmosa* (Radio Probing of the Earth Surface from Outer Space) (Compiled by M Nazirov, A P Pichugin, Yu G Spiridonov) (Leningrad: Gidrometeoizdat, 1990)
5. Nelepo B A et al. *Sputnikovaya Gidrofizika* (Earth Satellites and Hydrophysics) (Eds-in-Chiefs R Z Sagdeev, B A Nelepo) (Moscow: Nauka, 1983)
6. Kravtsov Yu A et al. *Issled. Zemli Kosmosa* (1) 3 (1996) [*Earth Obs. Rem. Sens.* **14** 1 (1996)]
7. Garbuk S V, Gershenzon V E *Kosmicheskie Sistemy Distantsionnogo Zondirovaniya Zemli* (Space-Based Systems for Remote Sensing of the Earth Surface) (Moscow: Inzhenerno-Tekhnol. Tsentr "SkanEks": A i B, 1997)
8. Kramer H J *Observation of the Earth and Its Environment. Survey of Missions and Sensors* 3rd ed. (Berlin: Springer-Verlag, 1996)
9. Alpers W R, Ross D B, Rufenach C L *J. Geophys. Res.* **86** 6481 (1981)
10. Bruening C, Alpers W R, Hasselmann K *Int. J. Remote Sensing* **1** 1695 (1990)
11. Kanevskiĭ M V, Novikov L V *Issled. Zemli Kosmosa* (4) 12 (1990)
12. Kanevsky M V *IEEE Trans. Geosci. Remote Sens.* **GE-31** 1031 (1993)
13. Kanevsky M V, in *Specialist Meeting on Microwave Remote Sensing, 5–9 Nov. 2001, Boulder, Colorado, USA*, Prog. and Abstracts, p. 2
14. Alpers W et al. *Issled. Zemli Kosmosa* (6) 83 (1994) [*Earth Obs. Remot. Sens.* **12** 903 (1995)]
15. Litovchenko K Ts et al. *Issled. Zemli Kosmosa* (3) 47 (1995)
16. Zaĭtsev V V, Litovchenko K Ts, Shirokov P A, in *Distantsionnye Metody Monitoringa Promyslovykh Raĭonov Mirovogo Okeana v Zadachakh Informatsionnoĭ Podderzhki Otraslevoĭ Nauchno-Proizvodstvennoĭ Deyatel'nosti* (Monitoring Commercially Important Regions of the World Ocean by Remote Sensing Techniques for Informational Support of Sectoral Research and Production Activities) (Ed. A A Romanov) (Moscow: Izd. VNIRO, 1997) p. 66
17. Wilde A, Bruening C, Alpers W *J. Geophys. Res.* **98** 6764 (1993)
18. Shutko A M *SVCh-Radiometriya Vodnoĭ Poverkhnosti i Pochvogruntov* (Microwave Radiometry of Water Surface, Ground and Soils) (Moscow: Nauka, 1986)
19. Wright J W *IEEE Trans. Antenn. Propag.* **AP-16** 217 (1968)
20. Valenzuela G R *Bound. Layer Meteorol.* **13** 61 (1978)
21. Beckmann P, Spizzichino A *The Scattering of Electromagnetic Waves from Rough Surfaces* (New York: Pergamon Press, 1963)
22. Bass F G, Fuks I M *Rasseyanie Voln na Statisticheski Nerovnoĭ Poverkhnosti* (Wave Scattering from Statistically Rough Surfaces) (Moscow: Nauka, 1972) [Translated into English (Oxford: Pergamon Press, 1979)]
23. Ishimaru A *Wave Propagation and Scattering in Random Media* Vols 1, 2 (New York: Academic Press, 1978) [Translated into Russian (Moscow: Mir, 1981)]
24. Rytov S M, Kravtsov Yu A, Tatarskiĭ V I *Vvedenie v Statisticheskuyu Radiofiziku* Vol. 2 *Sluchaĭnye Polya* (Introduction to Statistical Radiophysics Vol. 2 Random Fields) (Moscow: Nauka, 1978) [Translated into English: *Principles of Statistical Radiophysics* Vol. 3 *Elements of Random Fields* (Berlin: Springer-Verlag, 1988)]
25. Moore R K, Fung A K *Proc. IEEE* **67** 1504 (1979)
26. Kalmykov A I et al. *Izv. Vyssh. Ucheb. Zaved. Radiofiz.* **8** 1117 (1965)
27. Long M W *IEEE Trans. Antenn. Propag.* **AP-22** 667 (1974)
28. Longuet-Higgens M S *J. Fluid Mech.* **121** 403 (1982)
29. Malinovskiĭ V V *Morsk. Gidrofiz. Zh.* (6) 32 (1991)
30. Malinovskiĭ V V *Morsk. Gidrofiz. Zh.* (1) 53 (1993)
31. Kalmykov A I, Pustovoytenko V V *J. Geophys. Res.* **8**1 1960 (1976)
32. Lewis B L, Olin I D *Radio Sci.* **15** 815 (1980)
33. Walker D T et al. *Proc. R. Soc. London Ser. A* **452** 1953 (1996)
34. Kwoh D S W, Lake B M, Rungaldier H *J. Geophys. Res.: Oceans* **93** 12235 (1988)
35. Banner M L, Appl. Math. Preprint, AM 86/1 (Kensington, Australia: Univ. of New South Wales, 1985)
36. Wetzel L, in *Wave Dynamics and Radio Probing of the Ocean Surface* (Eds O M Phillips, K Hasselmann) (New York: Plenum Press, 1986) p. 273
37. Avanesova G G, Volyak K I, Shugan I V, in *Issledovaniya po Gidrofizike* (Hydrophysical Research) (Tr. Fiz. Inst. Akad. Nauk SSR, Vol. 156, Ed.-in-Chief F B Bunkin) (Moscow: Nauka, 1984) p. 94
38. Donelan M A, Pierson W J (Jr) *J. Geophys. Res.: Oceans* **92** 4971 (1987)
39. Trizna D B et al. *J. Geophys. Res.: Oceans* **96** 12529 (1991)
40. Trizna D B, in *Proc. of the IGARSS '93: 13th Intern. Geoscience and Remote Sensing Symp. Better Understanding of Earth Environment, Aug. 18–21, 1993, Tokyo, Japan* Vol. 2 (Ed. S Fujimura) (New York: IEEE, 1993) p. 776
41. McLaughlin D J et al. *IEEE J. Oceanic Eng.* **OE-20** 166 (1995)
42. Sletten M A, Trizna D B, Hansen J P *IEEE Trans. Antenn. Propag.* **AP-44** 646 (1996)
43. West J C, Sturm J M, Sletten M A, in *IGARSS '95. Quantitative Remote Sensing for Science and Applications: 1995 Intern. Geoscience and Remote Sensing Symp., July 10–14, 1995, Firenze, Italy* Vol. 3 (New York: IEEE, 1995) p. 2207
44. Kropfli R A, Clifford S F, in *Proc. of the IGARSS '94: Intern. Geoscience and Remote Sensing Symp. Surface and Atmospheric Remote Sensing: Technologies, Data Analysis, and Interpretation, Aug. 8–12, 1994, Pasadena, Calif., USA* Vol. 4 (Piscataway, NJ: IEEE, 1994) p. 2407
45. Lee P H Y et al. *IEEE Trans. Antenn. Propag.* **AP-44** 333 (1996)

46. Lee P H Y et al. *J. Geophys. Res.: Oceans* **100** 2591 (1995)
47. Guinard N W, Ransone J T, Daley J C *J. Geophys. Res.* **76** 1525 (1971)
48. Mityagina M I, Pungin V G, Yakovlev V V *Waves Random Media* **8** 111 (1998)
49. Kravtsov Yu A, Mityagina M I, Churyumov A N *Izv. Vyssh. Ucheb. Zaved. Radiofiz.* **XLII** (3) 240 (1999) [*Radiophys. Quantum Electron.* **42** 216 (1999)]
50. Kravtsov Yu A, Mityagina M I, Churyumov A N *Izv. Ross. Akad. Nauk. Ser. Fiz.* **63** 2403 (1999) [*Bull. Russ. Acad. Sci., Phys.* **63** 1859 (1999)]
51. Churyumov A N, Kravtsov Yu A *Waves Random Media* **10** 1 (2000)
52. Churyumov A N et al. *Adv. Space Res.* **29** 111 (2002)
53. Borovikov V A, Kinber B E *Geometricheskaya Teoriya Difraktsii* (Geometric Theory of Diffraction) (Moscow: Svyaz', 1978)
54. Kravtsov Yu A et al. *Vestn. Ross. Fonda Fundament. Issled.* (1) 32 (2001)
55. Kudryavtsev V N, Makin V K, Chapron B *J. Geophys. Res.: Oceans* **104** 7625 (1999)
56. Voronovich A G, Zavorotny V U *Waves Random Media* **11** 247 (2001)
57. Fuks I M, Voronovich A G *Waves Random Media* **9** 501 (1999)
58. Fuks I M, Voronovich A G, in *Proc. of the IGARSS '98: Sensing and Managing the Environment. 1998 IEEE Intern. Geoscience and Remote Sensing Symp., July 6–10, 1998, Seattle, WA, USA* Vol. 4 (Piscataway, NJ: IEEE, 1998) p. 2284
59. Naumenko M A et al. *Int. J. Remote Sensing* **15** 2039 (1994)
60. Bulatov M G et al. *Dokl. Ross. Akad. Nauk* **380** 816 (2001) [*Dokl. Earth Sci.* **381** 963 (2001)]
61. Hughes B A, Grant H L *J. Geophys. Res.: Oceans* **83** 443 (1978)
62. Basovich A Ya, Bakhanov V V, Talanov V N, in *Vozdeĭstvie Krupnomasshtabnykh Vnutrennikh Voln na Morskuyu Poverkhnost'* (The Action of Large-Scale Waves on the Sea Surface) (Ed.-in-Chief E N Pelinovskiĭ) (Gor'ky: Izd. IPF AN SSSR, 1982) p. 8
63. Plant W J *J. Geophys. Res.: Oceans* **102** 21131 (1997)
64. Zavorotny V U, Voronovich A G *IEEE Trans. Antenn. Propag.* **AP-46** 84 (1998)
65. Fung A K, Lee K K *IEEE J. Oceanic Eng.* **OE-7** 166 (1982)
66. Masuko H et al. *J. Geophys. Res.: Oceans* **91** 13065 (1986)
67. Vachon P W, Johannessen O M, Johannessen J A *J. Geophys. Res.: Oceans* **99** 22483 (1994)
68. Gossard E E, Richter J H, Atlas D *J. Geophys. Res.* **75** 3523 (1970)
69. Seitter K L, Muench H S *Mon. Weather Rev.* **113** 840 (1985)
70. Hoinka K P et al. *Tellus* **42A** 140 (1990)
71. Smith R K et al. *Mon. Weather Rev.* **123** 16 (1995)
72. Doviak R J, Zrnić D S *Doppler Radar and Weather Observations* 2nd ed. (San Diego, Calif.: Academic Press, 1993)
73. Smith R K, Page M A *Aust. Meteorol. Mag.* **33** 185 (1985)
74. Scherhag R, Berlin Weather Map, Supplement, 155/69 (Berlin: Free Univ. of Berlin, 1969)
75. Egger J *Meteorol. Rundsch.* **38** 103 (1985)
76. Eckard M, Fraedrich K *Meteorol. Rundsch.* **38** 119 (1985)
77. Shreffler J H, Binkowski F S *Mon. Weather Rev.* **109** 1713 (1981)
78. Gossard E E, Richter J H *J. Atmos. Sci.* **27** 971 (1970)
79. Doviak R J, Ge R *J. Atmos. Sci.* **41** 2559 (1984)
80. Drake V A *Bound. Layer Meteorol.* **31** 269 (1985)
81. Fulton R, Zrnić D S, Doviak R J *J. Atmos. Sci.* **47** 319 (1990)
82. Thomson R E, Vachon P W, Borstad G A *J. Geophys. Res.* **97** 14249 (1992)
83. Spiridonov Yu G, Pichugin A P, Shestopalov V P *Dokl. Akad. Nauk SSSR* **296** 317 (1987)
84. Alpers W, Stilke G *J. Geophys. Res.: Oceans* **101** 6513 (1996)
85. Kravtsov Yu A et al. *Issled. Zemli Kosmosa* (4) 3 (1997) [*Earth Obs. Rem. Sens.* **15** 513 (1999)]
86. Dolin L S, Rodin V V *Izv. Vyssh. Ucheb. Zaved. Radiofiz.* **23** (1) 79 (1980) [*Radiophys. Quantum Electron.* **23** 62 (1980)]
87. Zhidko Yu M, Kanevskiĭ M B, Rodin V V *Izv. Akad. Nauk SSSR. Fiz. Atmos. Okeana* **19** 328 (1983)
88. Kalmykov A I et al. *Dokl. Akad. Nauk SSSR* **279** 860 (1984)
89. Mitnik L M *La Mer* (3) 287 (1992)
90. Thompson T W, Liu W T, Wessman D E *J. Geophys. Res. Lett.* **10** 1172 (1983)
91. Fu L L, Holt B, Publ. 81–120 (Pasadena: Jet Propul. Lab., Calif. Inst. of Technol., 1983) p. 118
92. Ford J P, Cimino J B, Elachi C, Publ. 82–95 (Pasadena: Jet Propul. Lab., Calif. Inst. of Technol., 1983)
93. Vachon P W, Johannessen J A, in *Proc. of the IGARSS '94: Intern. Geoscience and Remote Sensing Symp. Surface and Atmospheric Remote Sensing: Technologies, Data Analysis, and Interpretation, Aug. 8–12, 1994, Pasadena, Calif., USA* Vol. 2 (Piscataway, NJ: IEEE, 1994) p. 802
94. Alpers W, Brummer B, in *Proc. of the IGARSS '93: 13th Intern. Geoscience and Remote Sensing Symp. Better Understanding of Earth Environment, Aug. 18–21, 1993, Tokyo, Japan* Vol. 2 (Ed. S Fujimura) (New York: IEEE, 1993) p. 540
95. Ufermann S, Romeiser R *J. Geophys. Res.: Oceans* **104** 25707 (1999)
96. Konyaev K V, Sabinin K D *Volny Vnutri Okeana* (Internal Waves in the Ocean) (St. Petersburg: Gidrometeoizdat, 1992)
97. Huges B A *J. Geophys. Res.* **83** 455 (1978)
98. Thompson D R *J. Geophys. Res.* **93** 12371 (1988)
99. Trokhimovskii Yu G *Izv. Akad. Nauk SSSR. Fiz. Atmos. Okeana* **32** 528 (1996) [*Izv., Atmos. Ocean. Phys.* **32** 488 (1996)]
100. Phillips O M *Izv. Akad. Nauk SSSR. Fiz. Atmos. Okeana* **9** 954 (1973)
101. Shugan I V, Voliak K I *Phys. Vibrations* **8** 79 (2000)
102. Basovich A Ya et al. *Izv. Akad. Nauk SSSR. Fiz. Atmos. Okeana* **22** 1194 (1986)
103. Kravtsov Yu A et al. *Radiotekhnika* (1) 61 (2000)
104. Etkin V S, Trokhimovski Yu G, Yakovlev V V, in *Proc. of the IGARSS '94: Intern. Geoscience and Remote Sensing Symp. Surface and Atmospheric Remote Sensing: Technologies, Data Analysis, and Interpretation, Aug. 8–12, 1994, Pasadena, Calif., USA* Vol. 2 (Piscataway, NJ: IEEE, 1994) p. 744
105. Kravtsov Yu A et al. *Issled. Zemli Kosmosa* (6) 43 (1997) [*Earth Obs. Rem. Sens.* **15** 909 (2000)]
106. Jansen R W et al., in *Proc. of the IGARSS '94: Intern. Geoscience and Remote Sensing Symp. Surface and Atmospheric Remote Sensing: Technologies, Data Analysis, and Interpretation, Aug. 8–12, 1994, Pasadena, Calif., USA* Vol. 1 (Piscataway, NJ: IEEE, 1994) p. 460
107. Jansen R W et al., in *Proc. of the IGARSS '93: 13th Intern. Geoscience and Remote Sensing Symp. Better Understanding of Earth Environment, Aug. 18–21, 1993, Tokyo, Japan* (Ed. S Fujimura) Vol. 2 (New York: IEEE, 1993) p. 550
108. Chubb S R et al. *IEEE Trans. Geosci. Remote Sens.* **GE-37** 1951 (1999)
109. Liu A K, in *Proc. of the IGARSS '93: 13th Intern. Geoscience and Remote Sensing Symp. Better Understanding of Earth Environment, Aug. 18–21, 1993, Tokyo, Japan* (Ed. S Fujimura) Vol. 2 (New York: IEEE, 1993) p. 547
110. Mitnik L M, Hsu M-K, Liu C-T *La Mer* **34** 215 (1996)
111. Mitnik L M, Hsu M-K, in *Proc. of the 4th Pacific Ocean Remote Sensing Conf. (PORSEC '98), Qingdao, China, July 28–31, 1998*, p. 416
112. Hovland H A, Johannessen J A, Digranes J, in *Proc. of the IGARSS '94: Intern. Geoscience and Remote Sensing Symp. Surface and Atmospheric Remote Sensing: Technologies, Data Analysis, and Interpretation, Aug. 8–12, 1994, Pasadena, Calif., USA* Vol. 4 (Piscataway, NJ: IEEE, 1994) p. 2038
113. Wahl T et al. *Coast. Management* **24** 61 (1996)
114. Wismann V et al. *Int. J. Remote Sensing* **19** 3607 (1998)
115. Schistad-Solberg A H et al. *IEEE Geosci. Remote Sensing* **GE-37** 1916 (1999)
116. Bern T-I et al. *Photogramm. Eng. Remote Sens.* **59** 423 (1993)